



AMERICAN METEOROLOGICAL SOCIETY

Journal of the Atmospheric Sciences

EARLY ONLINE RELEASE

This is a preliminary PDF of the author-produced manuscript that has been peer-reviewed and accepted for publication. Since it is being posted so soon after acceptance, it has not yet been copyedited, formatted, or processed by AMS Publications. This preliminary version of the manuscript may be downloaded, distributed, and cited, but please be aware that there will be visual differences and possibly some content differences between this version and the final published version.

The DOI for this manuscript is doi: 10.1175/2008JAS2768.1

The final published version of this manuscript will replace the preliminary version at the above DOI once it is available.



Aerodynamic contrails: Microphysics and optical properties

B. Kärcher,* B. Mayer, K. Gierens, U. Burkhardt, H. Mannstein,
and R. Chatterjee¹

Deutsches Zentrum für Luft- und Raumfahrt (DLR),

Institut für Physik der Atmosphäre, Oberpfaffenhofen, Germany

¹ National Institute of Technology, Trichirapalli, Tamil, Nadu, India

*Corresponding author address: Bernd Kärcher, Deutsches Zentrum für Luft- und Raumfahrt, Institut für

Physik der Atmosphäre, Oberpfaffenhofen, 82234 Wessling, Germany.

E-mail: bernd.kaercher@dlr.de

Abstract

Aerodynamic contrails form when air flows across the wings of subsonic aircraft in cruise. During a short adiabatic expansion phase, high supersaturations trigger burst-like homogeneous ice formation on ambient liquid aerosol particles within a wing depth. Small particles freeze first, because they equilibrate most rapidly. Ambient temperature is the key determinant of nascent aerodynamic contrail properties. Only above ~ 232 K, they become visible but are optically thin. These temperatures are at the high end of those prevailing at tropical upper tropospheric flight levels of subsonic aircraft. In colder midlatitude conditions, aerodynamic contrails stay invisible and the very small ice particles formed quickly evaporate when exposed to small subsaturations, explaining why the formation of these contrails is rarely observed. After formation, aerodynamic contrails develop into contrail cirrus if air is supersaturated with respect to ice. This type of anthropogenic ice clouds adds to contrail cirrus derived from jet exhaust contrails and may become particularly important in the future, as air traffic is projected to increase significantly in tropical and subtropical regions. Regardless of whether aerodynamically induced ice formation leads to persistent contrail cirrus, cruising aircraft may act as sources of potent heterogeneous ice nuclei by preactivating the insoluble fraction in atmospheric particle populations. Aerodynamic contrails and aerodynamically induced preactivation should therefore be studied experimentally and with global models to explore their potential to induce climate change.

1. Introduction

Mitigating the impact of aviation on climate change is becoming an increasingly important issue facing aviation industry and policy decision makers (Green 2005). Aircraft modify the Earth's climate by emitting carbon dioxide and nitrogen oxides and by producing persistent jet contrails under suitable meteorological conditions. Contrails forming from jet engine exhaust emissions increase the cirrus cloudiness and change the radiation budget significantly in regions with high air traffic density (Minnis 2003). The development of initially line-shaped contrails into cirrus clouds is not well understood, yet contrail cirrus may be the largest component in aviation radiative forcing (Sausen et al. 2005). Given the large uncertainty in evaluating the contrail climate impact despite almost two decades of scientific study (Forster et al. 2007), atmospheric research toward understanding the life cycle, spatial coverage, and microphysical and optical properties of contrail cirrus remains a high priority. Pending uncertainties must be significantly reduced before contrail mitigation strategies such as proposed by Mannstein et al. (2005) can be developed.

We suggest that aerodynamic triggering of upper tropospheric ice formation provides a previously unvalued source of anthropogenic contrail cirrus clouds and possibly preactivated efficient ice nuclei. Hence, we put aerodynamic contrails (Gierens et al. 2008) [hereafter Part I] up for discussion in the context of aircraft impacts on high cloudiness. Guided by observed aerodynamic contrail formation (Section 2), we estimate for the first time their formation conditions and initial properties by means of a simple order-of-magnitude analysis of time scales for microphysical and dynamical processes (Section 3) followed by a more detailed numerical analysis including sensitivity studies (Section 4). The latter enable us to make important inferences on the atmospheric relevance of aerodynamic contrails and contrail cirrus derived from

the former (Section 5). We highlight our key points in the summary (Section 6).

2. Observation

The commonly observed contrails form by mixing of jet engine exhaust with colder ambient air and become visible within one wing span behind the source aircraft. They initially appear as separate plumes behind each jet engine with a turbulent microstructure, expanding and quickly merging into line-shaped jet contrails upon entrainment of ambient air. Observed jet contrail formation is consistent with thermodynamic formation conditions (Schumann 1996) and their initial dynamical, chemical, and microphysical characteristics (Kärcher et al. 1996).

Figure 1 shows contrails produced by a wide-body aircraft cruising in the upper troposphere. According to National Centers for Environmental Prediction (NCEP) reanalysis data, the air temperature was ~ 241 K. We immediately recognize that jet contrails did not form behind the four jet engines. In fact, the ambient temperature is well above the maximum threshold value for formation of ~ 233 K (at ambient water saturation, 300 mb air pressure, and aircraft propulsion efficiency of 0.3). However, Fig. 1 shows two other distinct contrail features.

First, two thin lines emerge from the aircraft wing tips, which are soon captured by the rotating wing vortices. In these lines, condensation occurs due to rapid depression of air accelerated near the sharp tips. A similar effect is sometimes observed with turboprop aircraft at low altitudes in moist conditions, where condensation is caused by the tips of propeller blades turning at high speed. The rare appearance of wing tip contrails at cruise altitudes suggests that – besides being relatively warm – the air mass in which the aircraft flew had to be rather moist.

Second, a colorful, iridescent cloud sheet originates from the wing surfaces, as explained by

compressible fluid dynamics introduced in Part I. The white arrows in Fig. 1 associate distinct aerodynamic contrail colors with distances behind the wing. To convert these distances to time past formation, the distances should be divided by a typical cruising speed $U_0 \simeq 250$ m/s. This contrail becomes visible immediately behind the wings, first between the two innermost jet engines, and within a few meters later between the engines. Outside of the two outer engines, it does not appear. Contrary to the turbulent jet contrails, the nascent aerodynamic contrail initially exhibits a laminar structure.

Nascent jet contrails immediately appear bright and white, as turbulence mixes air parcels containing a high number density ($\sim 10^4 - 10^5$ cm $^{-3}$) of small (radii $\sim 0.5 - 1$ μ m) ice particles. Individual ice particles experience different growth histories, leading to a broadening of the particle size distribution (Paoli et al. 2004). By contrast, the sequence of colors in the aerodynamic contrail suggests rapid growth of nearly monodisperse particles, as we demonstrate in this study. After a distance of ~ 50 m, two linear features begin to appear in Fig. 1 that very much resemble ordinary jet contrails. Obviously, particles in the aerodynamic contrail created over the wing are mixed into the plumes and therefore begin to appear white.

3. Time scale analysis

a. Dynamical time scale

Figure 2 provides temperature histories of air parcels flowing over an idealized (Joukowski) wing of a wide-body aircraft in flight for various distances Δy above the wing surface at the leading edge, as calculated in Part I. For the selected trajectory closest to the wing ($\Delta y = 3.5$ m), T decreases by $\Delta T \simeq 15$ K below the ambient value $T_0 = 220$ K. The subscript 0 denotes

ambient values in the surrounding of the aircraft. This roughly corresponds to the relative temperature change $\Delta T/T_0 = (\gamma - 1)/\gamma \cdot (\Delta p/p_0)$ estimated with the adiabatic index $\gamma = 7/5$ and a pressure difference $\Delta p \simeq -50$ mb balanced by the weight of an aircraft cruising at $p_0 = 250$ mb, i.e., $\Delta T = -2T_0/35 \simeq -13$ K. Boundary layer effects are confined to a very narrow layer above the wing (Part I) and are not considered here.

The ratio of wing depth ($\Delta x \simeq 10$ m) to speed ($U_0 \simeq 250$ m/s) of an aircraft provides a dynamical time scale, $\tau_d = \Delta x/U_0 \simeq 40$ ms, associated with the formation phase of aerodynamic contrails. According to Fig. 1, these appear very close to the wing, so all microphysical processes responsible for their formation must evolve within τ_d (dynamical constraint). Typical cooling rates are of the order $\Delta T/\tau_d \simeq -0.5$ K/ms, similar to those found in jet contrails (Kärcher and Fabian 1994). Contrary to the steady decrease of T in jet contrails caused by isobaric mixing, a warming phase follows after cooling when the accelerated air flow slows its speed and approaches U_0 upon passing the trailing edge of the wing.

In Fig. 2, we also show the temporal development of the passive (without condensation or freezing) ice saturation ratio $S_i = nkT/e_i = e_i(T_0)/e_i(T)$. Here, n denotes the number concentration of H₂O molecules, $k = 1.38 \times 10^{-16}$ erg (gK)⁻¹ is the Boltzmann constant, and e_i is the saturation vapor pressure over ice, $e_i = 3.445 \times 10^{10} \exp(-\theta/T [\text{K}])$ mb, with $\theta = 6132.9$ K (Marti and Mauersberger 1993). The resulting high supersaturation triggers subsequent condensation and ice formation. For streamlines closer to the wing surface (but still above the turbulent boundary layer), saturation ratios reach values of ~ 40 , as shown later in this study.

From classical nucleation theory and a more detailed molecular model, the range of S_i -values at which ice nucleates homogeneously from the vapor phase is 50 – 90 (Pruppacher and Klett 1997). The maximum S_i -values are still below this range, underscoring the key role of

aerosols in generating the ice phase in aerodynamic contrails.

b. Microphysical time scales

An analysis of microphysical time scales relevant to aerodynamic contrail formation allows their basic properties to be estimated. We assume $p_0 = 250$ mb unless otherwise noted, corresponding to a typical cruise altitude. For convenience, we introduce a scaling factor $\kappa = p_0/p$ to track the dependences of our results on the ambient air pressure p . Cruising aircraft fly in a relatively narrow pressure regime (within 150 – 300 mb).

1) UPTAKE OF H₂O IN LIQUID AEROSOL PARTICLES

Particles containing supercooled aqueous solutions of sulfuric acid (H₂SO₄) and other components are suspended in ambient air flowing over aircraft wings. The mass fraction ω of water in an aerosol particle containing N H₂O molecules with mass m is $\omega = mN/(mN + M)^{-1}$, where M is the total mass of water-soluble substances. Over the very short time scale τ_d , only water condensation occurs ($M = \text{const.}$), because H₂O molecules are many orders of magnitude more abundant than any other condensable solute. The rate of change of ω in a liquid particle of radius r is then given by

$$\frac{d\omega}{dt} = \omega(1 - \omega) \frac{1}{N} \frac{dN}{dt}, \quad N = \frac{4\pi}{3v} r^3, \quad (1)$$

where $v \simeq 3 \times 10^{-23}$ cm³ is the volume of an H₂O molecule in solution. The H₂O uptake time scale τ_u follows from $\tau_u^{-1} = d \ln(\omega)/dt$, the characteristic time for changes in particle composition due to water uptake (dilution). It can also be interpreted as the time needed to approach local H₂O equilibrium between the gas phase and the liquid solution particle.

The number of H₂O molecules taken up in a cooling event per unit time in a liquid particle is determined by the diffusional flux (Pruppacher and Klett 1997)

$$\frac{dN}{dt} = 4\pi D\beta r \left(n - \frac{e}{kT} \right), \quad \beta^{-1} \simeq 1 + \frac{4D}{\alpha u r} = 1 + \frac{r_c}{r}, \quad (2)$$

where e is the water saturation vapor pressure over the solution droplet, $\beta \leq 1$ is a factor correcting the flux for gas kinetic effects, $u \propto \sqrt{T}$ is the mean thermal speed and $D \propto \kappa T^2$ is the gas diffusion coefficient of H₂O molecules, and $\alpha \simeq 1$ is their accommodation coefficient at the particle surface (Clement et al. 1996). The scaling of D with T is approximate. The characteristic radius r_c separates kinetic and diffusive uptake regimes. Values $r_c \propto \kappa T^{3/2}$ range between 0.55 – 0.75 μm . Underlying Eq.(2) is the assumption of a steady-state gas diffusion profile. This assumption is safe as steady-state conditions establish on a time scale $\sim r^2/D$, which is very much faster than any of the other time scales discussed in this work.

Recalling the discussion of Fig. 2 and assuming ambient ice saturation, we set $e(T) \ll nkT \simeq e_i(T_0)$ in Eq.(2). We approximate the water mass fraction at ice saturation by $\omega \approx 0.65$, a value typical for hygroscopic aerosols such as aqueous H₂SO₄ in the T -range considered here. Combining Eqs. (1) and (2) yields

$$\tau_u = 2.5 \times 10^{-11} \left(1 + 2 \times 10^{-4} \frac{\kappa T_0^{3/2}}{r_0} \right) \frac{r_0^2}{\kappa T_0} \exp\left(\frac{\theta}{T_0}\right), \quad (3)$$

giving τ_u in units of seconds for T_0 in K and r_0 in μm . For $\kappa = 1$ and $r_0 = 0.1 \mu\text{m}$, this leads to $\tau_u = 0.13 \text{ s}$, 0.011 s , and 0.002 s at $T_0 = 205 \text{ K}$, 220 K , and 235 K , respectively. For particles with $r_0 \ll r_c$ (kinetic regime), we obtain $\tau_u \propto r_0$, and for $r_0 \gg r_c$ (diffusion regime), $\tau_u \propto r_0^2$. The values τ_u increase almost exponentially with decreasing T_0 , because the equilibrium gas concentrations of H₂O decrease in proportion to e_i . Smaller particles are capable of responding faster than larger ones to changes in ambient relative humidity by taking up water; they simply need to condense fewer H₂O molecules per unit time to equilibrate.

2) HOMOGENEOUS FREEZING OF LIQUID AEROSOL PARTICLES

Homogeneous nucleation of ice in a supercooled aqueous particle occurs after sufficient H₂O molecules have been taken up, that is, when the water activity a in the particle becomes sufficiently large. Here, $a \leq 1$ is defined as the ratio of e and the saturation vapor pressure over a pure water particle. Homogeneous freezing is a threshold process, commencing at rather high ice saturation ratios ($S_* > 1.5$). The thresholds S_* depend on temperature and freezing particle size, but are independent of the chemical nature of the solute (Koop et al. 2000).

Starting at or near $S_i = 1$, freezing is expected after significant uptake of H₂O, that is, after τ_u . The trajectory in Fig. 2 with $\Delta y = 11.2$ m barely reaches S_* , implying that homogeneous freezing takes place within a wing depth above the wing surface ($\Delta y < \Delta x$). The increase in peak S_i with decreasing Δy implies that freezing rates are larger closer to the surface.

In the background atmosphere unaffected by the aircraft's flow field, liquid aerosol particles are in statistical equilibrium with the H₂O gas phase, except transiently in regions with large absolute cooling rates (> 30 K/h, in convective updrafts or lee waves). This is explained by τ_u -values much shorter (< 1 s for $T_0 > 200$ K) than time scales of most atmospheric processes creating non-equilibrium conditions in aerosols. Given the much higher cooling rates and the limited time τ_d available in the flow over airfoils, only liquid particles for which $\tau_u + \tau_f \leq \tau_d$ holds can participate in aerodynamic contrail formation, where τ_f is the homogeneous freezing time scale.

We derive τ_f in the Appendix (Eq.(A1)) and find that $\tau_f/\tau_d \simeq (4 - 8) \times 10^{-4} \ll 1$, and that τ_f is also much smaller than τ_u , except for extremely small r_0 of a few nm. Hence, τ_f is not a limiting factor in our analysis. The dynamical constraint then simplifies to $\tau_u \leq \tau_d$, or, using

Eq.(3):

$$r_0 \leq \hat{r}_0 = 10^{-4} \kappa T_0^{3/2} \left(\sqrt{1 + 4 \times 10^{15} \frac{\exp(-\theta/T_0)}{\kappa T_0^2} \tau_d} - 1 \right), \quad (4)$$

giving \hat{r}_0 in μm for T_0 in K and τ_d in ms. Values of \hat{r}_0 versus temperature are shown in Fig. 3 (upper solid curve) for $\kappa = 1$ and $\tau_d = 40$ ms. In full water equilibrium, the homogeneous freezing rate coefficient J is similar for all particles, and the rate JV rises with the liquid particle volume V . During aerodynamic contrail formation, particles larger than \hat{r}_0 have negligible J , because they lag behind equilibrium and stay at low a , so for them JV is small despite larger V . If particles become too small, water uptake is limited by the Kelvin barrier; an increased value of the saturation vapor pressure e prevents particles with $r_0 < r_K \simeq 4$ nm from freezing homogeneously in conditions favorable for contrail formation (Kärcher et al. 1995).

Figure 3 depicts the range of possible initial ice particle radii r_{i0} in aerodynamic contrails between the two solid curves, i.e., $r_K \leq r_{i0} \leq \hat{r}_0$. In the hatched areas, freezing of liquid particles is not possible, because either water uptake is too slow or the Kelvin barrier inhibits sufficient water uptake. Because freezing occurs almost instantaneously, τ_f is neglected and individual ice particles undergo an initial growth stage within their available time $\sim (\tau_d - \tau_u)$ according to the evolution of supersaturation depicted in Fig. 2.

If the homogeneous freezing temperature of activated aerosol particles (near 235 K) is not reached during adiabatic cooling, despite wing-induced peak cooling of the order 25 K, the aerodynamic contrail generated by a large aircraft would consist of (almost) pure water droplets and would only be stable in a water-saturated environment. For this to happen, T_0 must exceed 260 K, a condition not relevant for jet aircraft typically cruising above the 300 mb pressure level. At intermediate temperatures, aerodynamic contrails would be composed of layers of ice close to the wing followed by layers of liquid droplets higher above, but the liquid layer would rapidly

dissolve if the air is between water and ice saturation.

3) DEPOSITIONAL GROWTH OF ICE PARTICLES

The volume of an ice particle with radius r_i increases during deposition of H₂O molecules from the gas phase according to $v \cdot dN/dt$, which leads to the radial growth rate

$$\frac{dr_i}{dt} = \frac{v}{4\pi r_i^2} \frac{dN}{dt} = vD \frac{\beta_i}{r_i} \frac{e_i}{kT} s_i, \quad \beta_i^{-1} = 1 + \frac{r_c}{r_i}, \quad (5)$$

where we introduce the ice supersaturation $s_i = (S_i - 1)$ and use $\alpha_i = 1$, to compute r_c from Eq.(2). The flux in Eq.(5) approaches the maximum attainable gas kinetic limit $dN/dt = \alpha_i u \pi r_i^2 [n - e_i/(kT)]$, as the freshly nucleated ice particles are smaller than the mean free path of the H₂O molecules in air. The spherical approximation, neglect of the Kelvin effect, and the use of an upper limit value for molecular sticking is a good approximation for high supersaturation, in which case the role of migration of H₂O molecules to appropriate adsorption sites at the ice particle surface diminishes relative to vapor diffusion from the gas phase towards the ice particle. The vigorous growth under extremely high supersaturation is likely to produce amorphous ice. It would be interesting to learn more about the evolution of mass, shape, and structure of small ice particles created in this way once the supersaturation decayed to low ambient values.

We define the growth time scale by $\tau_g^{-1} = d \ln(r_i)/dt$, the characteristic time for a change in particle size due to water uptake. With $s_i > 0$, this time scale follows from Eq.(5):

$$\tau_g = 4 \times 10^{-11} \left(1 + 2 \times 10^{-4} \frac{\kappa T_0^{3/2}}{r_{i0}} \right) \frac{r_{i0}^2}{s_i \kappa T_0} \exp\left(\frac{\theta}{T_0}\right), \quad (6)$$

giving τ_g in seconds with r_{i0} in μm and T_0 in K. Setting $s_i = 1$ and identifying r_{i0} with the freezing aerosol particle radius r_0 for a rough estimate, we infer $\tau_g = \tau_u \cdot 3(1 - \omega)/\omega \simeq 1.6\tau_u$.

Hence, uptake and initial growth evolve over similar time scales.

The question arises whether the nascent ice particles with an initial radius $r_K \leq r_{i0} \leq \hat{r}_0$ and total concentration n_i affect the evolution of the H₂O number density n (or S_i) by vapor deposition. The rate of change is given by $dn/dt = -n_i dN/dt$. The time scale for relaxation of n toward equilibrium is given by $\tau_r^{-1} = -d \ln(n)/dt = 4\pi D \beta_i r_i n_i$ (combine Eqs.(2) and (5)), where n_i denotes the total ice particle number density and r_i the average ice particle radius. Inserting $r_i = r_{i0} = \hat{r}_0$ (largest possible initial radius) yields lower limit values for $\tau_r > 2500 \text{ cm}^{-3}/n_i$ in seconds for $T < 235 \text{ K}$. Because concentrations of upper tropospheric particles available for ice formation rarely exceed 2500 cm^{-3} (Schröder et al. 2002), $\tau_r > 1 \text{ s}$. Consequently, in the airflow over the wing, the evolution of S_i as shown in Fig. 2 is hardly affected by freezing and growth processes.

Integrating Eq.(5) with $T = T_0$ over the time Δt_f after freezing leads to

$$r_i(\Delta t_f) = r_c \left[\sqrt{1 + \left(\frac{r_{i0}}{r_c}\right)^2 \left(1 + 2\frac{r_c}{r_{i0}}\right) + 2\frac{vD}{r_c^2} \frac{e_i}{kT_0} \hat{s}_i \Delta t_f} - 1 \right], \quad (7)$$

where \hat{s}_i denotes the ice supersaturation averaged over Δt_f .

(i) *Initial growth stage*

We consider the early growth stage while air flows over the airfoil and the ice particles experience (most of) the supersaturation (Fig. 2). We approximate $\Delta t_f \approx \tau_d - \tau_u(r_{i0})$ and $\hat{s}_i \approx 5.5$ in Eq.(7), guided by a trajectory with $\Delta y = 3.5 \text{ m}$. The largest ice particles for which $\Delta t_f = 0$ form late and have no time left for growth, so $r_i(\Delta t_f) = r_{i0} = \hat{r}_0$. For smaller particles, Δt_f and $r_i(\Delta t_f)$ increases beyond r_{i0} ; their growth time is longer. At fixed r_{i0} , $r_i(\Delta t_f)$ -values strongly increase with T_0 , reflecting the exponential increase of the growth rate.

We recall that a short warming phase occurs after the supersaturation pulse around $x = 10$ m (Fig. 2), giving rise to subsaturations ($S_i \simeq 0.6$) over a time span $\sim \tau_d/2$. This warming causes some of the ice particles to evaporate. Its effect is visible in Fig. 1, where the aerodynamic contrail appears to fade out immediately behind the innermost parts of the wings, and then becomes better visible again due to further growth in ambient supersaturated air.

Small ice particles evaporate on a time scale $\tau_e = \tau_g(|s_i|)$ after their initial growth phase. The criterion for particles to survive evaporation during the transient warming is $\tau_e \geq \tau_d/2$, or, with Eq.(6):

$$r_{i0} \geq \hat{r}_i = 10^{-4} \kappa T_0^{3/2} \left(\sqrt{1 + 10^{15} \frac{\exp(-\theta/T_0)}{\kappa T_0^2} |s_i| \tau_d} - 1 \right), \quad (8)$$

giving \hat{r}_i in μm for T_0 in K and τ_d in ms. The values \hat{r}_i for $\kappa = 1$, $|s_i| = 0.4$, and $\tau_d = 40$ ms are shown as the dashed curve in Fig. 3. Ice particles formed below this limit that have not grown past \hat{r}_i evaporate. Hence, the stability region between the upper solid and the dashed curves, $\max\{r_K, \hat{r}_i\} \leq r_{i0} \leq \hat{r}_0$, includes ice particles that can undergo a second, atmospheric growth stage, provided the ambient air is supersaturated.

Particles interact with visible light of wavelength $\lambda \simeq 0.4 - 0.8 \mu\text{m}$ in the Mie scattering regime when the optical size parameter $2\pi r_i/\lambda \simeq 1$, i.e., for $r_i = r_v = \lambda/(2\pi) \simeq 100$ nm (arrow). Figure 3 demonstrates that only ice particles that either nucleated at a size above r_v or grew past r_v are large enough to be optically active in terms of Mie scattering.

We now address the question of how many ice particles form in aerodynamic contrails. Because $\tau_f \ll \tau_g$ and given the high supersaturations within τ_d , all available liquid particles in the region $r_K \leq r_{i0} \leq \hat{r}_0$ (Fig. 3) freeze. This minimizes the role of heterogeneous ice nuclei in aerodynamic contrail formation, because those constitute only a small subset of the total aerosol concentration (DeMott et al. 2003), justifying our approach that builds upon homoge-

neous freezing. While growing into the diffusion regime ($r_i > r_c$), any initial ice particle size distribution becomes very narrow, because according to Eq.(5), smaller particles grow faster. This is consistent with the appearance of colors in Fig. 1.

Concentrations of aerosol particles are highly variable in the upper troposphere, showing geographical and seasonal variations (Hofmann 1993), along with features caused by aerosol nucleation and cloud scavenging processes (Schröder et al. 2002). Total concentrations n_a usually exceed 500 cm^{-3} . Number mean radii r_a fall into the accumulation ($\sim 100 \text{ nm}$) or Aitken ($\sim 10 \text{ nm}$) mode size range. While an accumulation mode is always present, the Aitken mode is only populated near regions of active or recent nucleation.

We estimate the actual number density $n_f \leq n_a$ of freezing particles as a function of T_0 (via \hat{r}_0) from Eq.(4). To this end, we assume the aerosol size distribution to be unimodal and lognormal, with parameters n_a, r_a , and the geometric standard deviation σ_a (typical range 1.5 – 2). Concentrations of particles near the Kelvin radius r_K are usually small; as shown in the Appendix in Eq.(A2), those with $r_0 < \hat{r}_0$ are then approximated by

$$\frac{n_f}{n_a} \simeq \left[1 + \left(\frac{r_a}{\hat{r}_0} \right)^\delta \right]^{-1}, \quad \delta = \frac{4}{\sqrt{2\pi} \ln(\sigma_a)}. \quad (9)$$

This estimate together with Fig. 3 suggests that n_f falls well below n_a , if T_0 becomes sufficiently small. In such cases, the exact total number n_i of ice particles in aerodynamic contrails entering the stability region ($r_i > \hat{r}_i$) is more difficult to quantify; robust prediction of n_f depends on an accurate knowledge of the evolving freezing aerosol size distribution.

To address the question of visibility, we compute the initial temporal evolution of optical depth τ_v of a monodisperse ice particle population according to

$$\tau_v = \pi r_i^2 n_f Q_{\text{ext}}(r_i) \Delta y, \quad (10)$$

where r_i follows from Eq.(7) within $t = 0$ and $t = \tau_d - \tau_u(r_{i0})$, and $n_f \leq n_i$ is given by Eq.(9).

The Mie extinction efficiency at a given wavelength λ is approximated by (van de Hulst 1957)

$$Q_{\text{ext}} = 2 - \frac{4}{\varrho} \left[\sin(\varrho) - \frac{1 - \cos(\varrho)}{\varrho} \right], \quad \varrho = \frac{4\pi r_i (\mu - 1)}{\lambda}. \quad (11)$$

This formula is valid for refractive indices $1 > \mu > 2$ (we take $\mu = 1.31$ for ice and $\lambda = 0.55 \mu\text{m}$) and describes all salient features of the Mie extinction curve, being sufficiently accurate for our purpose. According to the discussion of S_i in Fig. 2, the geometrical aerodynamic contrail depth Δy is set equal to 5 m, about half of the peak wing depth of the airliner shown in Fig. 1. We define an approximate threshold optical depth of 0.01 for visibility, depending on human perception (Middleton 1952).

The temporal evolution of τ_v in the initial growth stage is depicted in Fig. 4 as a function of the scaled time available for growth after freezing, i.e., $0 \leq t/\Delta t_f \leq 1$, for $\tau_d = 40$ ms, $\kappa = 1$, $r_{i0} = r_a = 50$ nm, $\sigma_a = 2$, and four ambient temperatures T_0 including 241 K (see legend) relevant to the observation. To avoid maximizing τ_v in this order-of-magnitude analysis, we use a background particle number concentration $n_a = 500 \text{ cm}^{-3}$ at the low end of measurements and a low average supersaturation $\hat{s}_i = 2$, both accounting for transient subsaturations and spatial gradients in the flow field over the airfoil. These plausible choices are justified a posteriori by the numerical simulations shown in Fig. 5.

Only at the warmest T_0 the ice particles grow rapidly enough to become visible above the wing (curve crosses the approximate visibility threshold, dotted line in Fig. 4). Significantly below ~ 230 K, ice particles form but stay near their initial size most of the time (not shown). In addition, in the coldest case, n_i is already limited by small \hat{r}_0 -values of the order r_a (i.e., $n_f/n_a = 0.82$ at 210 K from Eq.(9)). This finding already hints at a basic explanation of the rare occurrence of visible aerodynamic contrails.

(ii) *Atmospheric growth stage*

After passing the airfoil, the ice particles continue to grow provided the ambient air is supersaturated, defining a second growth phase is required for contrail persistence. Before this atmospheric growth stage, the transient warming phase may reduce the ice particle concentration from Eq.(9). At low T_0 , the small ice particle sizes facilitate evaporation and render aerodynamic contrails less stable. In such cold conditions, they would not form if (small) Aitken mode particles were absent.

The r_i -values are largely controlled by T_0 rather than ambient S_i for times up to 1 s, or ~ 250 m distance behind the wing. Thereafter, $r_i(t)$ will be governed by a more complex evolution of T and S_i , as the aerodynamic contrail mixes with the jet plumes and the trailing vortices (see Fig. 1). We may expect that r_i -values then start to differ from each other significantly depending on wake dynamics and ambient supersaturation, but ice particles stay well below $1 \mu\text{m}$ for $T_0 < 210$ K.

In sum, particles smaller than \hat{r}_0 from Eq.(4) but larger than ~ 4 nm are expected to freeze instantaneously after τ_u from Eq.(3), because they equilibrate most rapidly and freezing occurs in a burst. The freezing process turns the available aerosol droplets into almost monodisperse, small ice particles that grow to sizes comparable to wavelengths of visible light and become visible above ~ 230 K. Further growth depends on levels of ambient supersaturation and details of plume and wake dynamics. Differences between jet exhaust and aerodynamic contrails are compiled in Tab. 1.

4. Numerical simulations

The above findings are illustrated and further explored by microphysical-optical simulations along trajectories of fluid parcels moving over different portions of an idealized airfoil. The microphysical model APSC m (Advanced Particle Simulation Code) used in this study is described in detail in Kärcher (2003). The size distributions provided by the microphysical model were input to an accurate Mie code (Wiscombe 1980) to calculate the spectral optical properties of the ice particles. Using a single scattering approximation, spectral radiance was estimated and converted to color. The limitations of the simple approximations in radiative transfer are discussed. The results of these calculations are compared with the observation from Fig. 1, which serves as the basis of our case study. Our results from Sect. 3 revealed that the ambient temperature is the sole key atmospheric factor influencing the properties of nascent aerodynamic contrails. Therefore, a sensitivity study is carried out to highlight aerodynamic contrail properties at different temperatures.

a. Case study

The observation of aerodynamic contrail formation discussed above forms the basis of our case study. In a first step, we performed aerodynamical simulations to calculate the flow and thermodynamic field above an idealized wing surface near the airframe. The wing depth was 11.7 m and the effective angle of attack was 1° (Part I). From this laminar flow field, we constructed a set of 20 streamlines stacked vertically above the wing, excluding the turbulent boundary layer the width of which does not exceed ~ 45 cm as estimated in Part I. Those were used as trajectories along which the APSC m was run to calculate aerosol and ice microphysics and

the water budget. Finally, the ice crystal size distributions were used to calculate the vertically integrated optical depth and served as input to a radiative transfer calculation to simulate the observed colors along the aging contrail.

According to the weather data, the ambient temperature and pressure was 241 K and 300 mb during the observation. In the absence of aerosol measurements, we used a total of 1000 cm^{-3} aqueous H_2SO_4 particles, distributed lognormally with a dry mean mass radius of 50 nm and a geometric width of 2. The corresponding wet aerosol spectrum is depicted in Fig. 6 (dashed curve). Ice crystals were treated as spheres. Particle growth rates due to water uptake were computed using mass accommodation coefficients of 1 and 0.5 for aerosol droplets and ice particles, respectively. All particles were transported along the streamlines, but nucleated aerosol particles were removed from the air parcels. To enable an atmospheric growth stage, the ambient air was assumed to be mildly supersaturated, $S_i = 1.1$. In fact, we have chosen this value to achieve a good agreement with the observation of colors in Fig. 1, given the other constraints noted above.

Figure 5 summarizes the results of the gasdynamical and microphysical calculations. Shown are S_i (top), n_i (bottom left), and the effective ice particle radius r_{eff} (bottom right), defined as the ratio of the third and second moment of the simulated ice particle size distribution. The ice saturation ratio resembles the results shown in Part I, in which water vapor was treated as a passive tracer in the flow field. This confirms that only a negligible amount of H_2O is taken up during aerosol freezing in the near-field area surrounding the wing (before the atmospheric growth stage). The highest ice supersaturation ratios of ~ 40 are achieved where adiabatic expansion is largest, as indicated by enhanced streamline curvatures within the region $\{x = 0 - 5 \text{ m}, y = 0 - 4 \text{ m}\}$. Successively lower S_i -values propagate upwards as the wing-induced

perturbations decay. Before and after the wing, some subsaturation is induced (darkest blue and black areas). The white contour curves separate subsaturated from supersaturated regions ($S_i = 1$), and regions in which ice particles can form ($S_i > 1.6$, see Sect. 3) or grow by vapor deposition ($S_i > 1$).

Freezing commences coincident with the sharp rise of S_i at the front of the airfoil. As predicted by our time scale analysis, in a region only few meters wide above the wing surface, most of the available aerosol particles freeze. The maximum ice particle concentration appears ~ 10 m (or ~ 40 ms) downstream of the zone where S_i takes its maximum, because aerosol particles need time to take up water in order to freeze (depending on particle size, this time τ_u may be of the order τ_d). About 10% of these crystals sublime in the subsaturated zone after passing the wing tail. The ice crystal concentrations fall off rapidly higher aloft, generating a sharp contrail lid after about half a wing depth. This behavior is consistent with the scaling of pressure, temperature, and relative humidity discussed in Part I. The effective ice particle sizes are largest near $x = 10$ m in a region 2 – 4 m above the wing, consistent with the fact that the maximum available condensable water maximizes there, as also shown in Part I. Below and above this region, r_{eff} -values are smaller because the ice particle number density is higher and supersaturation is lower, respectively.

Figure 6 presents the ice particle size distributions (solid curves) at selected times along the $y = 3.2$ m-trajectory (where the largest ice particles occur) and x -locations past the leading edge of the wing ($x = 0$). As expected, the first freezing particles are relatively small (~ 70 nm), although much larger droplets are available. Depositional growth becomes significant after a large portion of the aerosol particles have been transformed into ice, emphasizing the burst-like character of aerodynamic contrail formation. As estimated in the last section, the size

distribution becomes rapidly monodisperse, enabling the formation of colors. Together with the high concentrations, r_{eff} -values of the order $0.5 \mu\text{m}$ explain the immediate visibility of the contrail, in agreement with Fig. 1. The short warming after $x \simeq 10 \text{ m}$ forces r_{eff} to decrease in the subsaturated region, but the ice particles grow again in the atmospheric growth stage, because we have prescribed ambient supersaturation.

To simulate the colors for the resulting size distributions, the spectral scattering coefficient and scattering phase function were calculated using the Mie code. Scattering is most efficient when the ice particle radius equals the wavelength of the radiation ($r_i = \lambda$). The fact that the scattering properties depend on the ratio r_i/λ introduces a strong wavelength dependence (445 nm, 555 nm, and 600 nm representative for blue, green, and red), even though the refractive index of ice is nearly independent of λ in the visible spectral region. For particles with $r_i < 0.5 \mu\text{m}$, blue is scattered more than red, while this is reversed for larger sizes. For particles much larger than the wavelength, geometrical optics holds and the scattering coefficient no longer depends on wavelength. This illustrates the change in color as the ice particles grow.

Figure 7 shows the optical depth τ_v of the simulated aerodynamic contrail as a function of time, calculated by integrating the scattering coefficient over all vertical model layers. The optical depth increases rapidly to a first maximum of 0.012 once the ice crystals have finished the initial growth stage after $t \simeq 40 \text{ ms}$. Our simple estimate from Fig. 4 yields $\tau_v = 0.036$ as the first peak value at the same time for the case study. The difference between analytical estimate and simulated value arises mainly from the assumption of vertically uniform supersaturation and monodisperse ice particle concentration in the simple model. A transient decrease of τ_v forced by adiabatic warming and partial evaporation follows, after which τ_v is steadily rising again to 0.03 after $\sim 0.5 \text{ s}$ in the atmospheric growth stage. This evolution of τ_v is consistent

with Fig. 1 and our brief description provided in Sect. 2, suggesting that the assumed visibility threshold of 0.01 is meaningful. After 0.7 s, the ice crystal effective radius increases beyond $\sim 1 \mu\text{m}$, where Mie oscillations become important and modulate τ_v (not shown). Even slight deviations from spherical ice particle habits or surface roughness might modify τ_v from Fig. 4, but no simple means are available to assert such effects.

To calculate the colors displayed in Fig.7, a radiative transfer calculation was performed to simulate radiances in the visible spectral range. As a first approximation, the color of the scattered radiation was calculated with a simple single scattering approximation; the spectral scattering coefficient was multiplied with the spectral extraterrestrial irradiance. Hence we neglect the wavelength-dependence of the scattering phase function, as well as the contribution of Rayleigh scattering. The consequences of this simplified treatment are discussed below. The approximate spectral radiances were converted into colors following the procedure by CIE (1986). In brief, spectral radiance (calculated with a step width of 5 nm within $\lambda = 380 - 780 \text{ nm}$) is multiplied with the three color matching functions and integrated to obtain the tristimulus values X, Y, and Z, which are in turn converted to color (R,G,B) values using the CIE system matrix. Brightness is considered by multiplying (R,G,B) with the luminosity Y.

The resulting colors are shown in Fig. 7 as a function of time. They can be divided into three main regions, again consistent with Fig. 1: up to 0.3 s (75 m), colors are mostly blue, in the range 0.3 – 0.7 s (75 – 175 m) yellow and orange, and after 0.7 s (175 m) mostly pink, roughly comparing to the colors on the photograph except for the yellow region that appears to start with green in Fig. 1, which is not simulated.

As mentioned above, this is only a rough approximation. An exact calculation would require detailed knowledge about the geometry of the scene, in particular the viewing direction

of the camera. In the following, we present a refined calculation including Rayleigh scattering and molecular absorption and discuss the consequences for the interpretation. To simulate radiances, we use the libRadtran radiative transfer model (Mayer and Kylling 2005) with the discrete ordinate solver DISORT (Stamnes et al. 1988). libRadtran has been shown to produce accurate sky radiances, in particular for cloudy conditions (Mayer et al. 2004). The conversion from spectral radiance to colors is performed as described above. Two simplifications were introduced: As the effective ice particle radii r_{eff} vary only little with height above the wing, we used r_{eff} of the layer with the largest ice water content and applied it for all heights. The vertically integrated optical depth τ_v was set to 0.03 for this calculation.

We need to consider that in Fig. 1 not only the age of the contrail changes, but also the viewing angle. From the observation data (vertical distance 1200 m, length of the contrail 175 m), we estimate that the contrail spans about 10° in the image, which needs to be considered in the calculation. As an example, Fig. 8 shows the radiance distribution along two directions: (a) along the principal plane of the sun (relative azimuth 0° ; this plane is defined by the direction of incident sunlight and the vertical direction); and (b) perpendicular to the principal plane of the sun (relative azimuth 90°); both as a function of time. The horizontal axis is the time t after the aircraft, the vertical axis the viewing zenith angle θ . The images show the distribution of radiance over the full viewing angle, as if the sky was completely covered by the simulated contrail. (In our one-dimensional radiative transfer simulation, the contrails fills the whole sky.) Absolute brightness is not considered for the plots; rather, the colors were normalized, because the result is much brighter in the vicinity of the sun and the other regions would not be visible at all. The solar zenith angle was -40° , marked by the white line in Fig. 8a. If the aircraft in the photograph flew along the principle plane, the trajectory would resemble the dotted black line

in Fig. 8a, starting at $\theta = -35^\circ$ (close to the sun) and heading directly away from the sun. In reality, the aircraft trajectory could be any straight line starting at a $t = 0$ and ending at $\theta = 10^\circ$ higher or lower in the vertical. The real trajectory was probably neither in the principle plane nor perpendicular, but somewhere in between. Figure 8c finally shows the colors along the trajectory from Fig. 8a. The colors in this example are close to the observation, but they depend on the viewing geometry and the orientation of the flight path. In particular, the sequence of colors is very similar to our simple approximation in Fig. 7.

It is immediately obvious that the colors are slightly affected by the viewing geometry, as the exact colors are determined not only by the extinction coefficient but also by the details of the scattering phase function. Since the scattering phase function has a strong forward peak, the most interesting effects appear in the vicinity of the sun, where the scattering by the ice particles dominate over the Rayleigh scattering. Nevertheless, the sequence of colors is always similar, irrespective of where we place the aircraft path in Fig. 8a. However, the contrast is strongly affected by the viewing geometry. The contrail is clearly visible close to the sun, but the further away from the sun, the less can the contrail be distinguished from the blue sky, because the sideward scattering by the contrail particles is much smaller than in the forward direction and a much larger optical depth would be required for the contrail to become visible against the blue Rayleigh background. In the perpendicular plane, only little is to be seen, because the viewing directions in the perpendicular plane are always more than 40° away from the sun.

From these studies we conclude that a contrail with $\tau_v = 0.01 - 0.03$ should be clearly visible from the flight altitude of the lower aircraft. The colors, however, appear only if the contrail is observed close to the sun. If observed from the ground, the Rayleigh scattering between surface and aircraft further reduce the contrast and a larger optical depth is probably

required to clearly distinguish the contrail.

We do not overemphasize the discussion of colors at this point for two further reasons. First, slight alterations of plume turbulence or background meteorological parameters also affect the colors, as suggested by Fig. 1 of Part I. Second, photographs and their reproduction are not fully conservative with respect to colors.

b. Sensitivity study

We performed a sensitivity study by changing T_0 for otherwise unchanged parameters. Figure 9 shows the simulated temporal evolution of r_{eff} for the case study (241 K) and three lower temperatures. The transient warming phase is most clearly observed for the highest T_0 where growth and evaporation rates are fastest. While r_{eff} -values grow past $0.1 \mu\text{m}$ at the two warmest temperatures, this is hardly the case for 220 K and not at all for 210 K. The labels in Fig. 9 indicate the simulated ice water contents after 1 s of contrail age. Only above 230 K are these values comparable to those in jet exhaust contrails, which are always visible at the time of formation; at lower temperatures aerodynamic contrails become extremely tenuous. The simulations also predict that the number of nucleated ice crystals decreases when T_0 decreases, because slower water uptake rates prevent particles from freezing. These numerical results are entirely consistent with the estimates from the analytical study in Section 3.

We briefly explore the consequences of these results for optical depth at $\lambda = 0.5 \mu\text{m}$ and a contrail age of 0.7 s. At solar wavelengths, τ_v scales in proportion to the ratio of ice water content (IWC) and r_{eff} for constant extinction efficiency (Fu and Liou 1993). For the case study at $T_0 = 241 \text{ K}$, we have $\tau_v \simeq 0.03$, $r_{eff} \simeq 1 \mu\text{m}$ and $\text{IWC} \simeq 1 \text{ mg m}^{-3}$, yielding the approximate relationship $\tau = 0.03 \cdot \text{IWC}/r_{eff}$ by setting $Q_{\text{ext}} = 2$ despite r_{eff} -values of the

order λ . For $T_0 = 230$ K, 220 K, and 210 K we find $r_{eff} = 0.43 \mu\text{m}$, $0.2 \mu\text{m}$, and $0.07 \mu\text{m}$ read off Fig. 9 and $\text{IWC} = 0.12 \text{ mg m}^{-3}$, 0.009 mg m^{-3} , and 0.0002 mg m^{-3} from our simulations, respectively. Taken together, τ_v decreases to 0.008, 0.001, and 9×10^{-5} with decreasing temperature, extending our earlier results from Fig. 4 into the atmospheric growth stage to a distance of ~ 175 m (0.7 s) behind the wing. We further estimate that nascent aerodynamic contrails become invisible once the temperature falls below ~ 232 K, explaining why they are difficult to observe.

Reductions or enhancements of ambient ice supersaturation would slow or enhance the atmospheric growth stage, but leave the formation process unaffected. If fewer liquid-containing aerosol particles were available than assumed here, aerodynamic contrails would initially contain somewhat larger ice crystals.

5. Atmospheric relevance

Similar to jet contrails, the evolution of aerodynamic contrails depends on details of how the wing-induced contrail sheet is captured by and trapped in the trailing aircraft vortices and on the subsequent decay of these vortices (Lewellen and Lewellen 2001). Figure 1 demonstrates that aerodynamic contrails become at least partly captured in the jet plumes and vortices. Wake vortex dynamics can lead to a substantial loss of jet contrail ice crystals depending on a wide range of ambient conditions and aircraft parameters (Unterstrasser et al. 2008). This is consistent with a large variability in surviving ice particle concentrations found in contrails of a few minutes of age (Schröder et al. 2000). If the capturing process is less effective for aerodynamic contrails, then the surviving fraction may be larger than for jet contrails. Given sufficient time for aging

in supersaturated air, we suspect that it will be difficult to distinguish visually contrail cirrus created by the aerodynamical process from contrail cirrus derived from jet exhaust, because the ice water content in persistent contrails of either source will quickly be dominated by condensed ambient water. Regardless, we suggest to study the interaction between jet plumes and aerodynamic contrails in the aircraft wake up to the atmospheric dispersion regime (~ 5 min after formation) in more detail in the future, both experimentally and with advanced computational fluid dynamics methods.

a. Aerodynamic contrail cirrus

To judge the atmospheric relevance of aerodynamic contrails, we discuss temperatures measured along the flight paths of commercial airliners based on five years of Measurement of Ozone and Water Vapor by Airbus In-Service Aircraft (MOZAIC) data. Figure 10 displays the mean temperature values in different pressure layers along with the average overall layers in ice-supersaturated regions allowing contrails to persist. In the extratropics ($> 30^\circ\text{N}$), mean tropospheric temperatures cover the range 211.5–221 K, averaging to ~ 218 K at ~ 230 mb. In the tropics ($0 - 30^\circ\text{N}$), temperatures are significantly higher: 218.5 – 234 K, averaging to ~ 228 K at ~ 235 mb. Therefore, the occurrence frequency of aerodynamic contrails is expected to be much higher in the tropics than at middle and high latitudes.

The region enclosed by the dotted lines in Fig. 10 marks the range of threshold temperatures below which jet exhaust contrails can form, assuming ambient ice saturation. While temperatures are very often low enough to enable jet contrail formation at midlatitudes, they would not form in the majority of cases in lower latitudes. (We recall that the contrail from Fig. 1 has been observed near 32°N at a rather high temperature too warm for the generation of jet con-

trails.) This demonstrates that large regions exist in which aerodynamic contrails can provide a complementary source of contrail cirrus.

The impact of aerodynamic contrails on the radiation balance depends on the evolution of their optical depth and coverage. After decay of the wake vortices, ice water path and effective ice particle size of contrail cirrus are governed by atmospheric temperatures and factors including moisture supply and wind shear, among others. Optical properties of contrail cirrus are different from those of natural cirrus because of different formation conditions.

As aerodynamic contrails preferably form at warm temperatures in low latitudes and the ice water content is a strong function of temperature (Schumann 2002) [his Fig. 11.5 showing a compilation of field data], they should result in optically thicker contrail cirrus than those existing in extratropical latitudes. In tropical and subtropical areas, mean vertical shear of the horizontal wind vector $\partial_z \vec{v}$ in the upper troposphere calculated from daily climate model data appears to be larger than at middle latitudes due to large instantaneous directional wind shear (Burkhardt and Becker 2006) [their Figs. 1(c) and (d) displaying dissipative heating rates $\propto (\partial_z \vec{v})^2$]. This presumably increases aerodynamic contrail cirrus coverage and decreases ice water path faster in the tropics. Warmer temperatures and larger ice water content tend to generate larger ice crystals, reducing the effect of aerodynamic contrail cirrus by limiting their lifetimes due to enhanced ice crystal sedimentation.

Current subsonic air traffic is low in the tropical areas, but in the future, air traffic is expected to increase strongly in these regions. Between 30°N and 30°S at 300 mb, the frequency of ice supersaturation is $\sim 10\%$ with maxima located over Africa and the Maritime Continent, but jet contrail formation conditions are seldomly met (Burkhardt et al. 2008). Hence, the fraction of persistent aerodynamic contrail cirrus is likely to increase significantly. The resulting global

radiative forcing by aerodynamic contrails is expected to be different from current estimates of radiative forcing by jet contrails. Without prognostic models that enable the simulation of interactions between contrail cirrus, water vapor and natural cirrus cloud fields, and because of the complex microphysical mechanisms affecting the properties and coverage of contrail cirrus, these differences in radiative forcing will be difficult to predict and quantify.

b. Aerodynamically-induced preactivation

Another aspect concerns the microphysical processing of aerosol particles flowing over airfoils. The insoluble fraction in atmospheric particle populations is forced to form sub-micrometer ice particles in all conditions where ice is generated aerodynamically, that is, according to our discussion, essentially across all subsonic flight levels. This processing may be viewed as a specific type of preactivation – ice may form on these preactivated nuclei at lower supersaturations than without processing. Preactivation of exhaust soot particles may also occur after dissolution of short-lived jet contrails (Kärcher et al. 2007). Virtually nothing is known in general about preactivation in cirrus conditions, but it is possible that aerodynamic ice formation provides a low temperature source of effective ice nuclei. We attempt to provide a very rough estimate of the number concentration n_{pre} of preactivated ice nuclei. This value should be compared to recent estimates of the background concentration of upper tropospheric heterogeneous ice nuclei from in-situ measurements in the northern hemisphere of some 0.01 cm^{-3} (DeMott et al. 2003; Haag et al. 2003).

The value of n_{pre} is given by the product of the number concentration of available insoluble particles at cruise levels n_{ins} capable of serving as preactivation nuclei, which may be some 10 cm^{-3} according to aircraft measurements (Minikin et al. 2003), and the ratio between the air

volume processed by aerodynamic ice formation V_{pre} and the upper tropospheric volume V_{trop} in which air traffic is mainly concentrated. The latter is approximated by the zonal band within 30°N and 60°N between 9 – 12 km altitude, $V_{trop} \simeq 2.8 \times 10^8 \text{ km}^3$. We assume rapid mixing of aerodynamically processed air within V_{trop} .

The processed air volume may be computed as the product of the initial aerodynamic contrail cross section $A \simeq 100 \text{ m}^2$ and the aircraft flight path L . The current fleet travels a total distance of $\sim 2.75 \times 10^9 \text{ km}$ globally per month; from this number, fractions of 0.9 and 0.75 are flown in the northern hemisphere and upper troposphere, respectively. Using monthly flown distance accounts for the fact that the mean residence time of upper tropospheric air is of the order of four weeks. This yields $L \simeq 1.9 \times 10^9 \text{ km}$ and $V_{pre} \simeq 1.9 \times 10^5 \text{ km}^3$, combining to $n_{pre} = n_{ins} V_{pre} / V_{trop} \simeq 0.007 \text{ cm}^{-3}$. This value is uncertain because it is not known how many insoluble particles can actually be preactivated, how often the same air mass is processed several times, and because of spatial inhomogeneities of the flight routes neglected here. Nevertheless, it is possible that aerodynamically-induced preactivation contributes with some significance to the apparent background concentration of effective heterogeneous ice nuclei, possibly already affecting natural cirrus formation. This contribution likely increases in the future given projected increases in air traffic growth rates.

6. Summary

We have presented the first detailed investigation of the formation and initial evolution of aerodynamic contrails based on an observation. Formation conditions have been studied using analytical tools based on an order-of-magnitude analysis of time scales for microphysical and

dynamical processes. A numerical simulation model has been adapted and employed along with radiative transfer calculations to unravel the microphysical and optical evolution of aerodynamic contrails. Their properties have been contrasted with those of the more commonly observed jet exhaust contrails.

One key finding is that aerodynamic contrails need high temperatures – at the high end of those prevailing at low latitude subsonic flight levels – to form stable ice crystals capable of developing into contrail cirrus in supersaturated air masses. This serves as the main explanation for their rare observability during formation. Because jet contrails hardly form in such conditions, the aerodynamic triggering of ice formation provides a hitherto unrecognized source of anthropogenic contrail cirrus clouds with distinct optical properties. This source may become particularly important in the future, as air traffic is forecasted to increase mainly in southeast and east Asia, where temperatures at flight altitudes are high enough.

At temperatures prevailing at midlatitude subsonic flight levels, it is unlikely that aerodynamic contrails develop into contrail cirrus. However, every cruising aircraft is a potential source of potent ice nuclei via preactivation of ambient insoluble particles. Aerodynamic preactivation is virtually unaffected by ambient conditions and should occur very frequently, contributing with some significance to the background concentration of heterogeneous ice nuclei in cirrus conditions. Whether preactivation is effective depends on the chemical and morphological nature of ambient insoluble particles and their behavior when exposed to very short pulses of extremely high supersaturations. Laboratory studies would be a viable option to address this issue.

In view of the potential importance of aerodynamic contrails and aerodynamically induced preactivation, we suggest to perform in-situ measurements of aerodynamic contrails in condi-

tions favorable for their formation and persistence. Our study serves as a useful guide to design such experiments that would ideally employ airborne lidar instruments (Uthe et al. 1998). Airborne and remote sensing observations should include instruments to measure relative humidity and microphysical and optical properties of small ice crystals accurately. Such observations would provide valuable data in support of global modeling. Besides achieving a better understanding of jet contrails, it is of interest to study the potential impact of aerodynamic contrails on the current and future climate using climate models including a physically-based representation of contrail-related processes.

Acknowledgments.

This work was carried out within the DLR-projects PAZI-2 and CATS.

APPENDIX

Homogeneous freezing time scale

The ice particle production rate during homogeneous freezing can be approximated by $dn_i/dt \equiv \dot{n}_i(t) = \dot{n}_i(t_0) \exp[-(t - t_0)/\tau_f]$. Here, n_i is the ice particle number density and $\tau_f^{-1} = d \ln(\dot{n}_i)/dt$ defines the freezing time scale. The time t_0 varies from $-\infty$ far ahead of the wing to $+\infty$ far behind the wing. As $\dot{n}_i = JVn_a$ (n_a denotes the freezing particle number density), τ_f contains two components stemming from the freezing rate coefficient J

and the freezing particle volume $V = 4\pi r^3/3$. The component which varies most quickly is $J = J[T(t)]$, resulting in $\tau_f^{-1} = d\ln(J)/dt \simeq \partial\ln(J)/\partial T \cdot dT/dt$.

The freezing rate JV must be high enough to freeze a liquid particle with a typical radius $r_0 = 50$ nm within τ_d , i.e., $J_* = 3/(4\pi r_0^3 \tau_d) \simeq 5 \times 10^{16}$ cm⁻³/s. We compute $\partial\ln(J)/\partial T$ for $J = J_*$, i.e., for $a = \text{const.}$ at which $S_i = S_*$. We obtain $\partial\ln(J)/\partial T \simeq (300 - 2T)$ K⁻¹ with T between 180 – 240 K as a rough approximation, ignoring the dependence on r_0 via J_* . Substituting $dT/dt \simeq \Delta T/\tau_d$ finally yields

$$\tau_f = \frac{8.75}{\kappa T_0 (T_0 - 150)} \tau_d, \quad (\text{A1})$$

with T_0 in K.

Freezing particle fraction

The fraction f_* of particles larger than a threshold radius r_* in a lognormal size distribution with mode radius r_a and standard deviation σ_a is given by

$$f_* = \frac{1}{\sqrt{2\pi} \ln(\sigma_a)} \int_{r_*}^{\infty} \exp\left[-\frac{\ln^2(r/r_a)}{2 \ln^2(\sigma_a)}\right] \frac{dr}{r} = \frac{1}{2} [1 - \text{erf}(z)], \quad z = \frac{\ln(r_*/r_a)}{\sqrt{2} \ln(\sigma_a)}.$$

Using an accurate approximation for the error function, $\text{erf}(z) \simeq \tanh(2z/\sqrt{\pi})$, we obtain

$$1 - \text{erf}(z) \simeq \frac{2}{1 + \exp(4z/\sqrt{\pi})} = \frac{2}{1 + (r_*/r_a)^\delta}, \quad \delta = \frac{4}{\sqrt{2\pi} \ln(\sigma_a)}.$$

The fraction of particles in the range $[r_K, r_*]$ is then finally given by

$$f \simeq \left[1 + \left(\frac{r_K}{r_a}\right)^\delta\right]^{-1} - \left[1 + \left(\frac{r_*}{r_a}\right)^\delta\right]^{-1}, \quad (\text{A2})$$

with r_K being the minimum radius below which particles cannot freeze due to the Kelvin barrier.

When identifying r_* with $\hat{r}_0 \geq r_K$ from Eq.(4), Eq.(A2) approximately describes the fraction of particles in the ambient aerosol size distribution that is likely to freeze in aerodynamic contrails.

References

- Burkhardt, U. and E. Becker, 2006: A consistent diffusion-dissipation parameterization in the ECHAM climate model. *Mon. Wea. Rev.*, **134**, 1194–1204.
- Burkhardt, U., B. Kärcher, M. Ponater, K. Gierens, and A. Gettelman, 2008: Contrail cirrus supporting areas. *Geophys. Res. Lett.*, **35**, doi:10.1029/2008GL034056, in press.
- CIE, 1986: *Standard on Colorimetric Observers*. Commission Internationale de l’Eclairage (CIE), CIE S002 ed.
- Clement, C. F., M. Kulmala, and T. Vesala, 1996: Theoretical considerations on sticking probabilities. *J. Aerosol Sci.*, **27**, 869–882.
- DeMott, P. J., D. J. Cziczo, A. J. Prenni, D. M. Murphy, S. M. Kreidenweis, D. S. Thomson, R. Borys, and D. C. Rogers, 2003: Measurements of the concentration and composition of nuclei for cirrus formation. *Proc. Natl. Acad. Sci.*, **100**, 14,655–14,660.
- Forster, P., V. Ramaswamy, P. Artaxo, T. Berntsen, R. Betts, D. Fahey, J. Haywood, J. Lean, D. Lowe, G. Myhre, J. Nganga, R. Prinn, G. Raga, M. Schulz, and R. V. Dorland, 2007: Changes in Atmospheric Constituents and in Radiative Forcing. in: *Climate Change 2007: The Physical Science Basis. Contribution of Working Group 1 to the 4th Assessment Report of the Intergovernmental Panel on Climate Change*. [Solomon, S., D. Qin, M. Manning, Z. Chen, M. Marquis, K. B. Averyt, M. Tignor and H. L. Miller (eds.)], Cambridge University Press, Cambridge, UK, and New York, USA.

- Fu, Q. and K. N. Liou, 1993: Parameterization of the radiative properties of cirrus clouds. *J. Atmos. Sci.*, **50**, 2008–2025.
- Gierens, K., B. Kärcher, H. Mannstein, and B. Mayer, 2008: Aerodynamic contrails: Phenomenology and fluid dynamics. *J. Atmos. Sci.*, **65**, submitted.
- Green, J. E., 2005: Future aircraft – greener by design? *Meteorol. Z.*, **14**, 583–590.
- Haag, W., B. Kärcher, J. Ström, A. Minikin, U. Lohmann, J. Ovarlez, and A. Stohl, 2003: Freezing thresholds and cirrus cloud formation mechanisms inferred from in situ measurements of relative humidity. *Atmos. Chem. Phys.*, **3**, 1791–1806.
- Hofmann, D. J., 1993: Twenty years of balloon-borne tropospheric aerosol measurements at Laramie, Wyoming. *J. Geophys. Res.*, **98**, 12,753–12,766.
- Kärcher, B., 2003: Simulating gas-aerosol-cirrus interactions: Process-oriented microphysical model and applications. *Atmos. Chem. Phys.*, **3**, 1645–1664.
- Kärcher, B. and P. Fabian, 1994: Dynamics of aircraft exhaust plumes in the jet regime. *Ann. Geophysicae*, **12**, 911–919.
- Kärcher, B., O. Möhler, P. DeMott, S. Pechtl, and F. Yu, 2007: Insights into the role of soot aerosols in cirrus cloud formation. *Atmos. Chem. Phys.*, **7**, 4203–4227.
- Kärcher, B., T. Peter, U. M. Biermann, and U. Schumann, 1996: The initial composition of jet condensation trails. *J. Atmos. Sci.*, **53**, 3066–3083.
- Kärcher, B., T. Peter, and R. Ottmann, 1995: Contrail formation: Homogeneous nucleation of H₂SO₄/H₂O droplets. *Geophys. Res. Lett.*, **22**, 1501–1504.

- Koop, T., B. P. Luo, A. Tsias, and T. Peter, 2000: Water activity as the determinant for homogeneous ice nucleation in aqueous solutions. *Nature*, **406**, 611–614.
- Lewellen, D. and W. Lewellen, 2001: The effect of aircraft wake dynamics on contrail development. *J. Atmos. Sci.*, **58**, 390–406.
- Mannstein, H., P. Spichtinger, and K. Gierens, 2005: A note on how to avoid contrail cirrus. *Transp. Res.*, **10**, 421–426.
- Marti, J. and K. Mauersberger, 1993: A survey and new measurements of ice vapor pressure at temperatures between 170 and 250 K. *Geophys. Res. Lett.*, **20**, 363–366.
- Mayer, B. and A. Kylling, 2005: Technical Note: The libRadtran software package for radiative transfer calculations: Description and examples of use. *Atmos. Chem. Phys.*, **5**, 1855–1877.
- Mayer, B., M. Schröder, R. Preusker, and L. Schüller, 2004: Remote sensing of water cloud droplet size distributions using the backscatter glory: A case study. *Atmos. Chem. Phys.*, **4**, 1255–1263.
- Middleton, W. E. K., 1952: *Vision Through The Atmosphere*. University of Toronto Press, Toronto.
- Minikin, A., A. Petzold, J. Ström, R. Krejci, M. Seifert, P. van Velthoven, H. Schlager, and U. Schumann, 2003: Aircraft observations of the upper tropospheric fine particle aerosol in the northern and southern hemispheres at midlatitudes. *Geophys. Res. Lett.*, **25**, 1339–1342.
- Minnis, P., 2003: *Contrails*. In: *Encyclopedia of Atmospheric Sciences*. J. Holton, J. Pyle and J. Curry (Eds.), Academic Press, London, 509–520 pp.

- Paoli, R., J. Hélie, and T. Poinso, 2004: Contrail formation in aircraft wakes. *J. Fluid Mech.*, **502**, 361–373.
- Pruppacher, H. R. and J. D. Klett, 1997: *Microphysics of Clouds and Precipitation*. Kluwer Acad. Pub., Dordrecht.
- Sausen, R., I. Isaksen, V. Grewe, D. Hauglustaine, D. Lee, G. Myhre, M. O. Köhler, G. Pitari, U. Schumann, F. Stordal, and C. Zerefos, 2005: Aviation radiative forcing in 2000: An update on IPCC (1999). *Meteorol. Z.*, **14**, 555–561.
- Schröder, F., B. Kärcher, C. Duroure, J. Ström, A. Petzold, J.-F. Gayet, B. Strauss, P. Wendling, and S. Borrmann, 2000: The transition of contrails into cirrus clouds. *J. Atmos. Sci.*, **57**, 464–480.
- Schröder, F., B. Kärcher, M. Fiebig, and A. Petzold, 2002: Aerosol states in the free troposphere at northern midlatitudes. *J. Geophys. Res.*, **107** (8126), doi:10.1029/2000JD000194.
- Schumann, U., 1996: On conditions for contrail formation from aircraft exhausts. *Meteorol. Z.*, **5**, 4–23.
- , 2002: *Contrail cirrus*. In: *Cirrus*. Eds. D. K. Lynch, K. Sassen, D. O’C. Starr and G. Stephens. New York, Oxford Univ. Press, 346–374 pp.
- Spichtinger, P., 2004: Eisübersättigte Regionen. Dissertation (in German), Research Report DLR-FB 2004-21, Deutsches Zentrum f. Luft- u. Raumfahrt.
- Stamnes, K., S. Tsay, W. Wiscombe, and K. Jayaweera, 1988: A numerically stable algorithm for discrete-ordinate-method radiative transfer in multiple scattering and emitting layered media. *Appl. Opt.*, **27**, 2502–2509.

Unterstrasser, S., K. Gierens, and P. Spichtinger, 2008: The evolution of contrail microphysics in the vortex phase. *Meteorol. Z.*, **17**, 145–156.

Uthe, E. E., N. Nielsen, and T. Osberg, 1998: Airborne scanning lidar observations of aircraft contrails and cirrus clouds during success. *Geophys. Res. Lett.*, **30 (1503)**, doi:10.1029/2002GL016458.

van de Hulst, H. C., 1957: *Light Scattering by Small Particles*. John Wiley, New York.

Wiscombe, W., 1980: Improved Mie scattering algorithms. *Appl. Opt.*, **19**, 1505–1509.

List of Figures

- 1 Photograph of a contrail-producing Airbus A340 aircraft cruising at 9600 m altitude, close to a pressure level of 300 mb and a temperature of 241 K as estimated from NCEP reanalysis data. The photo was taken from a second aircraft 1200 m below on the same route over eastern China on June 12, 2005, from 14:59 to 15:06 Beijing time (\sim 07:00 UTC). Both aircraft were heading to NW from ($32^{\circ}14.8'N$, $119^{\circ}46.7'E$) to ($32^{\circ}56.8'N$, $119^{\circ}10.1'E$). The white bar marks the length scale, guided by the wing span (\sim 60 m) of the airliner. Its wing depth is \sim 11 m. Any length scale can be converted to approximate times using a typical cruising speed of 250 m/s, i.e., 60 m correspond to 0.24 s. The arrows and associated distances mark distinct color regimes appearing after the wing (blue/violett, green/yellow, pink/white). Photo adapted from <http://www.airliners.net/> courtesy of pilot Jeff Well (personal communication, 2007). 41
- 2 Evolution of temperature T and ice saturation ratio S_i along trajectories of air parcels flowing over a wing near the fuselage of a large aircraft in flight. Ambient values are 220 K and 1, respectively. Values are shown as a function of distance x flown or approximate time t elapsed. The hatched area marks the location of the wing, the leading (trailing) edge of which is located at $x = 0$ (11.7) m. Legend indicates distances of air parcels above the wing surface at the leading edge. 42

3	Radii of smallest (r_K) and largest (\hat{r}_0) freezing aerosol particles in aerodynamic contrails (upper and lower solid curves, respectively) as a function of ambient temperature T_0 . In the hatched region, ice particles cannot form above the wing surface. Ice particles below the dashed curve (\hat{r}_i) likely evaporate when air warms while passing the leading edge of the wing. Arrow marks the approximate radius r_v at which the scattering efficiency becomes large.	43
4	Evolution of visible optical depth τ_v of aerodynamic contrails as a function of the normalized time t available for initial (within $\tau_d - \tau_u$) depositional growth after freezing for different ambient temperatures T_0 (curves) along with a visibility threshold (dotted line). Legends indicate T_0 -values.	44
5	Distribution of ice saturation ratio S_i (top), ice particle number density n_i (bottom left), and ice particle effective radius r_{eff} (bottom right) over a wing of a wide-body airliner. Ambient conditions as in Fig. 1 with 10% supersaturation over ice. Two white contour curves are explicitly shown in the S_i -plot. Thin black curves represent selected streamlines.	45
6	Size distributions of aerosol (dashed) and ice particles (solid) along the trajectory located ~ 3.2 m above the wing corresponding to Fig. 5. Shown is the initial wet aerosol size spectrum along with selected ice crystal spectra. Labels on the latter indicate distances past the leading edge of the wing and corresponding times elapsed.	46
7	Evolution of visible optical depth τ_v and the appearance of colors as a function of time t after the air has passed the leading edge of the wing. Color sequence can be compared to Fig. 1.	47

- 8 Simulated radiances in the principal plane (a) and perpendicular to the principle plane (b) as a function of time t and viewing zenith angle θ . Colors are identical for viewing zenith angle 0° , where the viewing direction is identical (nadir). Thick white line marks the position of the sun, the dotted black line is one of many possible aircraft flight paths; (c) color sequence along the dotted black line. 48
- 9 Temporal evolution of effective ice particle radii r_{eff} for different ambient temperatures T_0 including the case study. Values have been taken along the $y = 3.2$ m trajectory. Labels denote the simulated ice water content at $t = 1$ s. . 49
- 10 Mean temperatures T (circles) measured onboard commercial aircraft based on MOZAIC data (1995-1999). Data are taken in ice-supersaturated regions covering the tropics ($0 - 30^\circ\text{N}$) and the northern extratropical upper troposphere and lowermost stratosphere. Labels 1, 2, 3, 4 correspond to pressure layers 190 – 209 mb, 210 – 230 mb, 231 – 245 mb, and 246 – 270 mb, respectively, and label ‘avg’ denotes the average over all layers. Average values have been weighted by the number of flights occurring in each layer. Temperatures are approximately normally distributed and the bars denote one standard deviation. The region between the two dotted lines marks the range of threshold temperatures below which jet contrails form in ice-saturated air within 190 – 270 mb and using a propulsion efficiency of 0.3. Figure adapted from Spichtinger (2004). 50

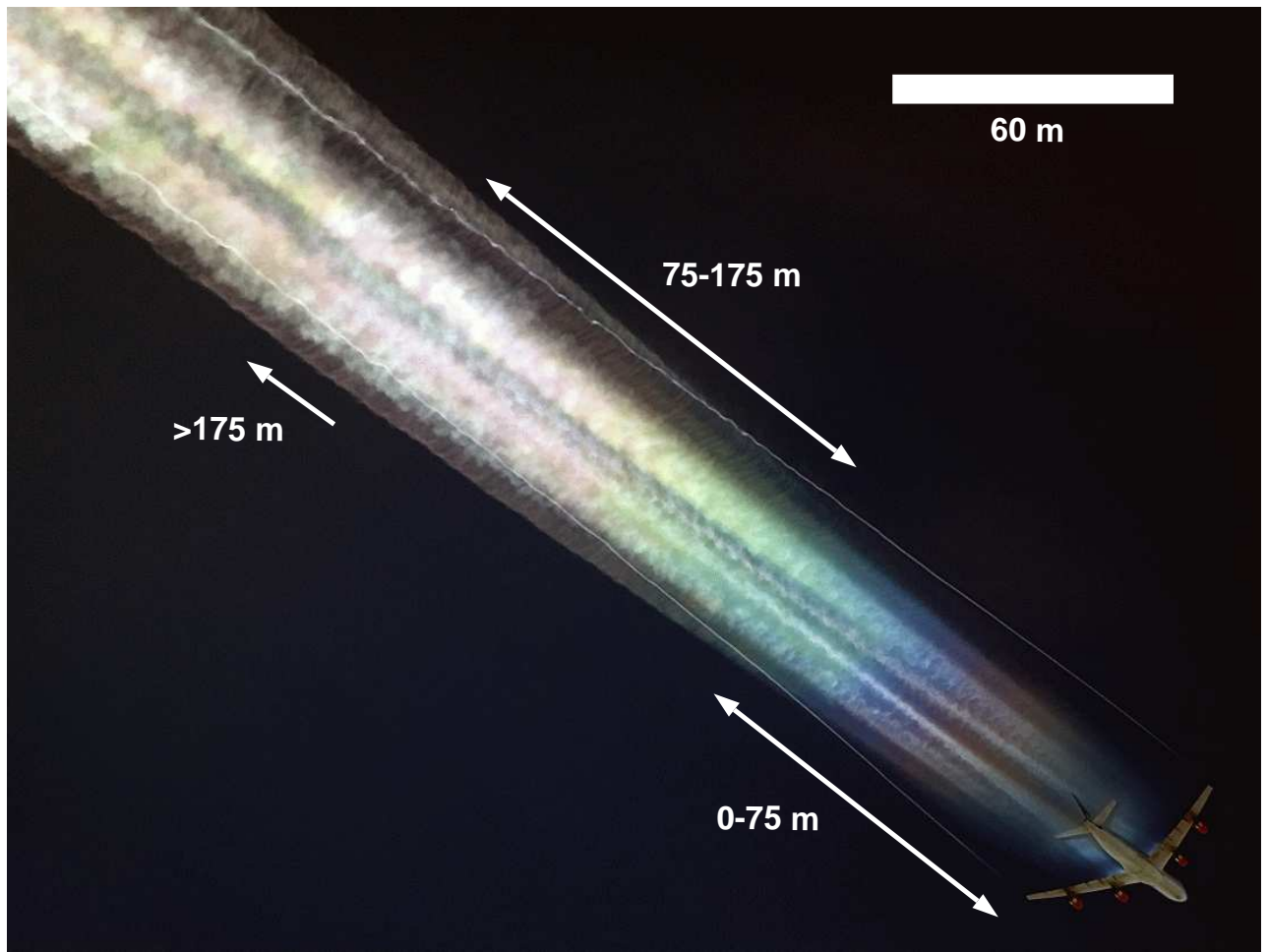


FIG. 1. Photograph of a contrail-producing Airbus A340 aircraft cruising at 9600 m altitude, close to a pressure level of 300 mb and a temperature of 241 K as estimated from NCEP reanalysis data. The photo was taken from a second aircraft 1200 m below on the same route over eastern China on June 12, 2005, from 14:59 to 15:06 Beijing time (\sim 07:00 UTC). Both aircraft were heading to NW from ($32^{\circ}14.8'N$, $119^{\circ}46.7'E$) to ($32^{\circ}56.8'N$, $119^{\circ}10.1'E$). The white bar marks the length scale, guided by the wing span (\sim 60 m) of the airliner. Its wing depth is \sim 11 m. Any length scale can be converted to approximate times using a typical cruising speed of 250 m/s, i.e., 60 m correspond to 0.24 s. The arrows and associated distances mark distinct color regimes appearing after the wing (blue/violet, green/yellow, pink/white). Photo adapted from <http://www.airliners.net/> courtesy of pilot Jeff Well (personal communication, 2007).

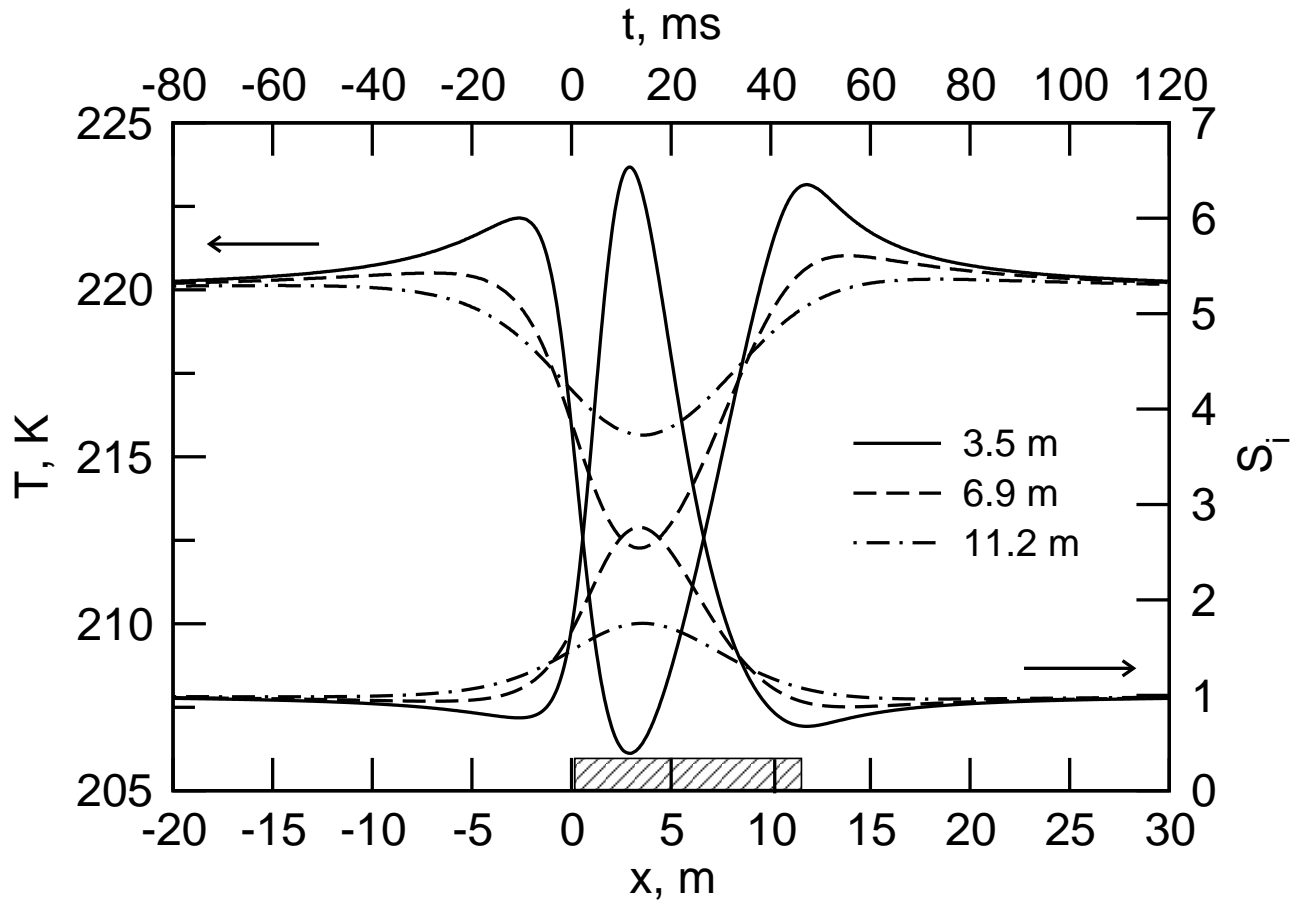


FIG. 2. Evolution of temperature T and ice saturation ratio S_i along trajectories of air parcels flowing over a wing near the fuselage of a large aircraft in flight. Ambient values are 220 K and 1, respectively. Values are shown as a function of distance x flown or approximate time t elapsed. The hatched area marks the location of the wing, the leading (trailing) edge of which is located at $x = 0$ (11.7) m. Legend indicates distances of air parcels above the wing surface at the leading edge.

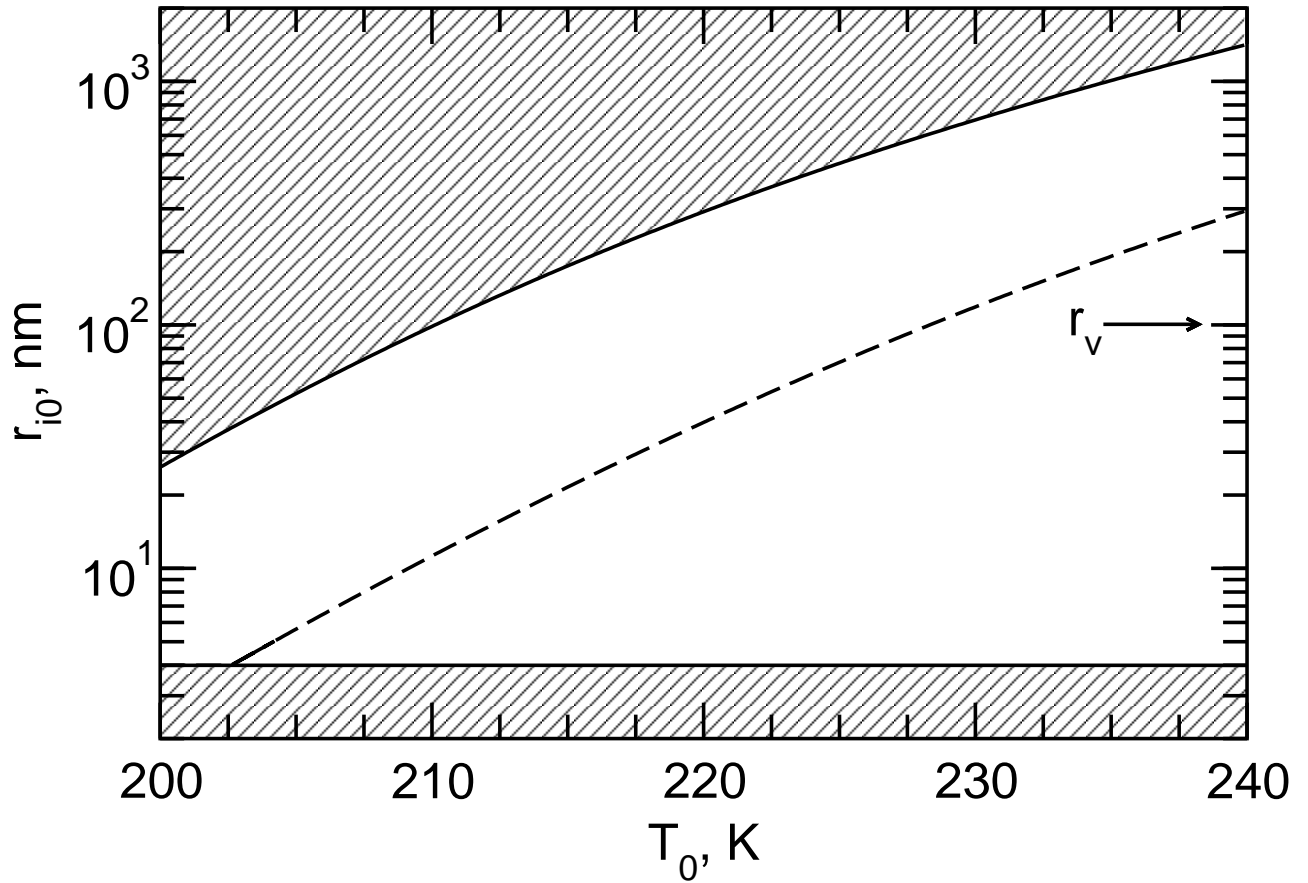


FIG. 3. Radii of smallest (r_K) and largest (\hat{r}_0) freezing aerosol particles in aerodynamic contrails (upper and lower solid curves, respectively) as a function of ambient temperature T_0 . In the hatched region, ice particles cannot form above the wing surface. Ice particles below the dashed curve (\hat{r}_i) likely evaporate when air warms while passing the leading edge of the wing. Arrow marks the approximate radius r_v at which the scattering efficiency becomes large.

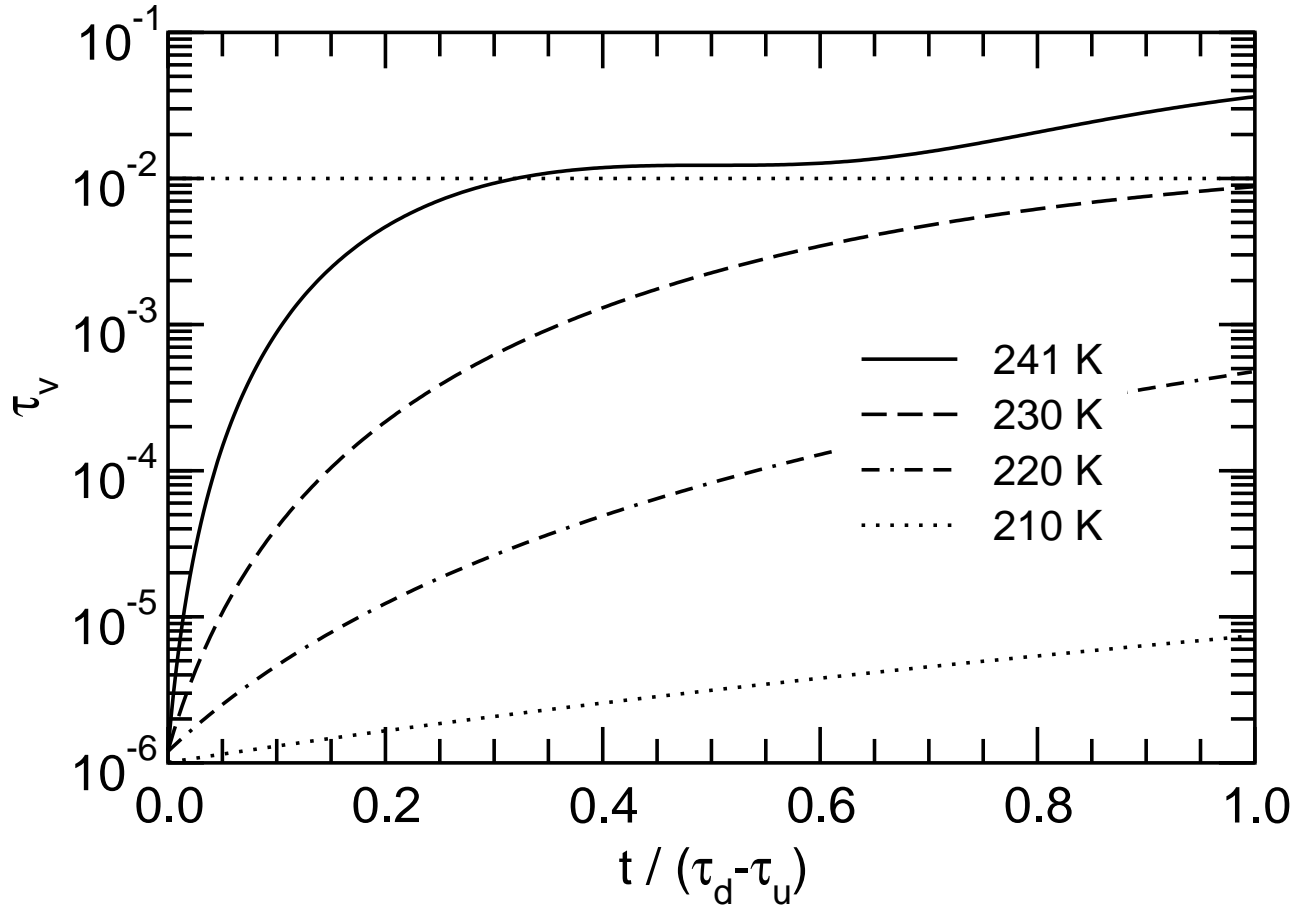


FIG. 4. Evolution of visible optical depth τ_v of aerodynamic contrails as a function of the normalized time t available for initial (within $\tau_d - \tau_u$) depositional growth after freezing for different ambient temperatures T_0 (curves) along with a visibility threshold (dotted line). Legends indicate T_0 -values.

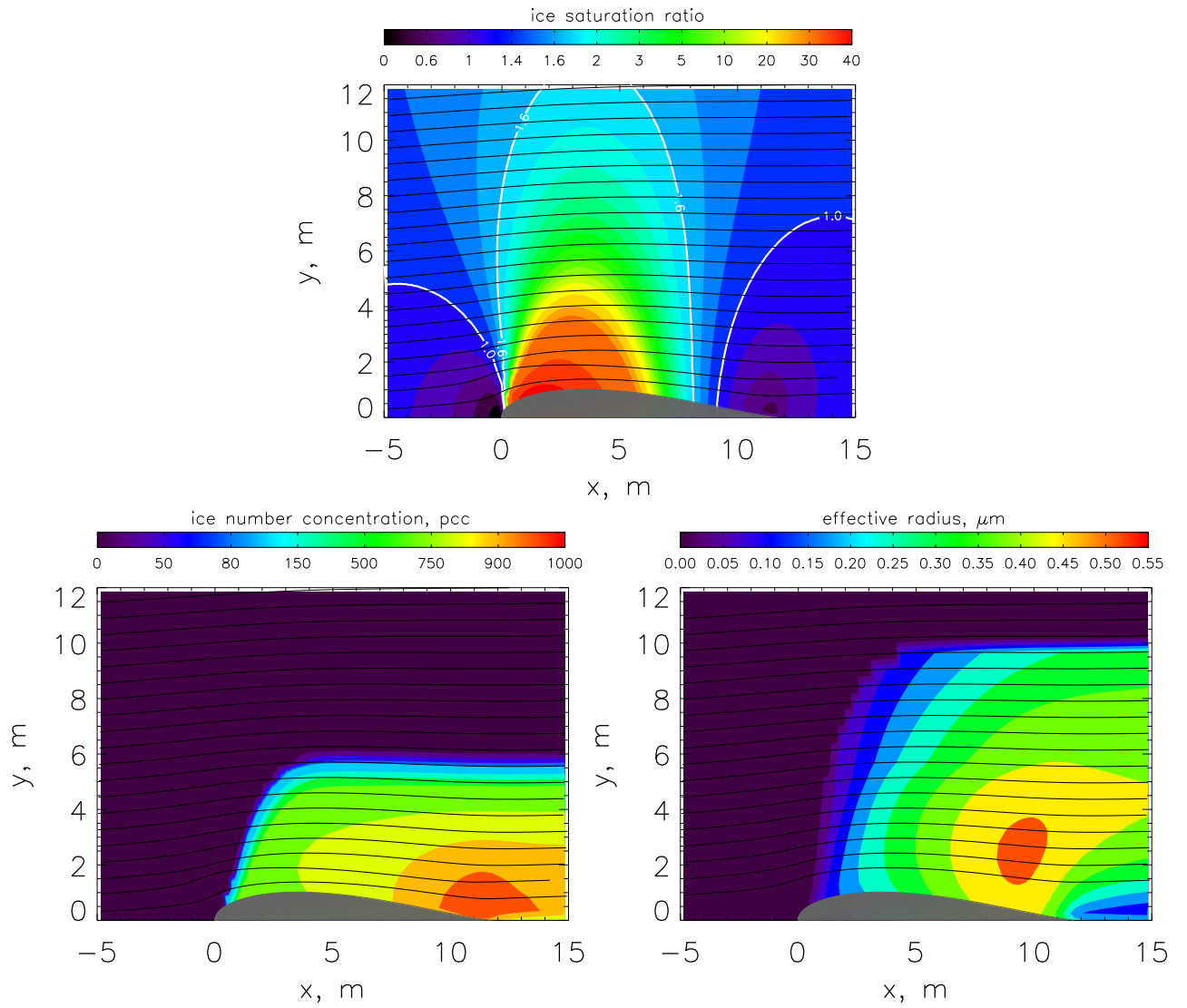


FIG. 5. Distribution of ice saturation ratio S_i (top), ice particle number density n_i (bottom left), and ice particle effective radius r_{eff} (bottom right) over a wing of a wide-body airliner. Ambient conditions as in Fig. 1 with 10% supersaturation over ice. Two white contour curves are explicitly shown in the S_i -plot. Thin black curves represent selected streamlines.

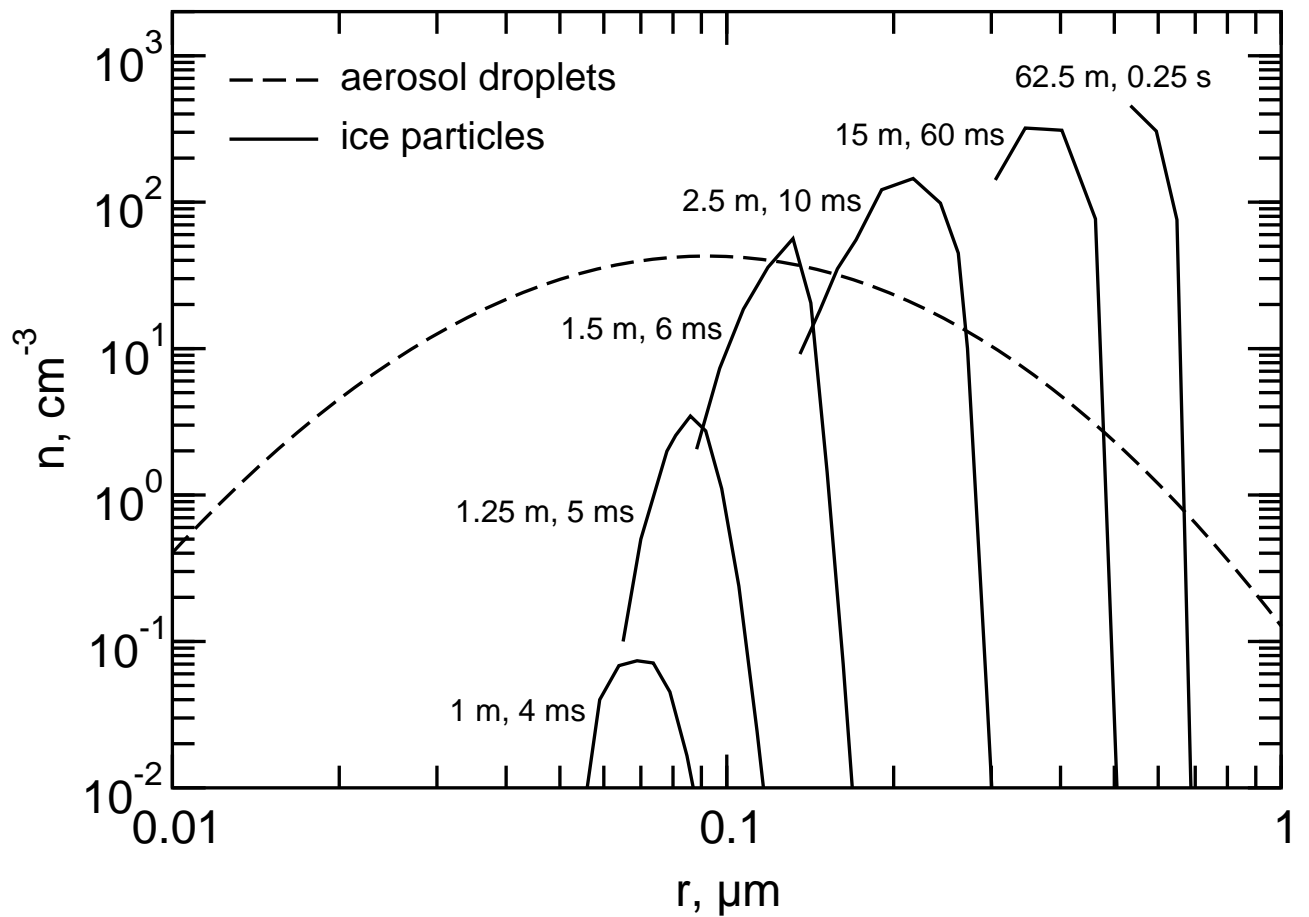


FIG. 6. Size distributions of aerosol (dashed) and ice particles (solid) along the trajectory located ~ 3.2 m above the wing corresponding to Fig. 5. Shown is the initial wet aerosol size spectrum along with selected ice crystal spectra. Labels on the latter indicate distances past the leading edge of the wing and corresponding times elapsed.

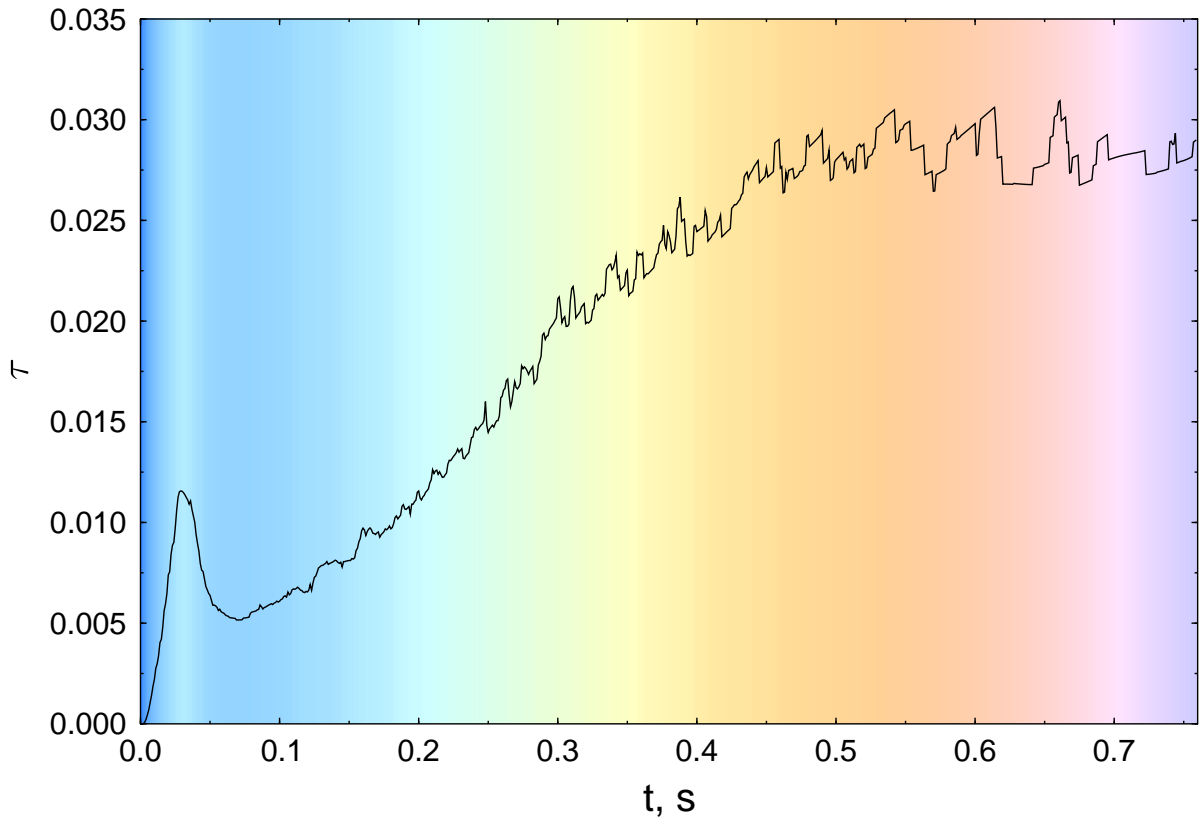


FIG. 7. Evolution of visible optical depth τ_v and the appearance of colors as a function of time t after the air has passed the leading edge of the wing. Color sequence can be compared to Fig. 1.

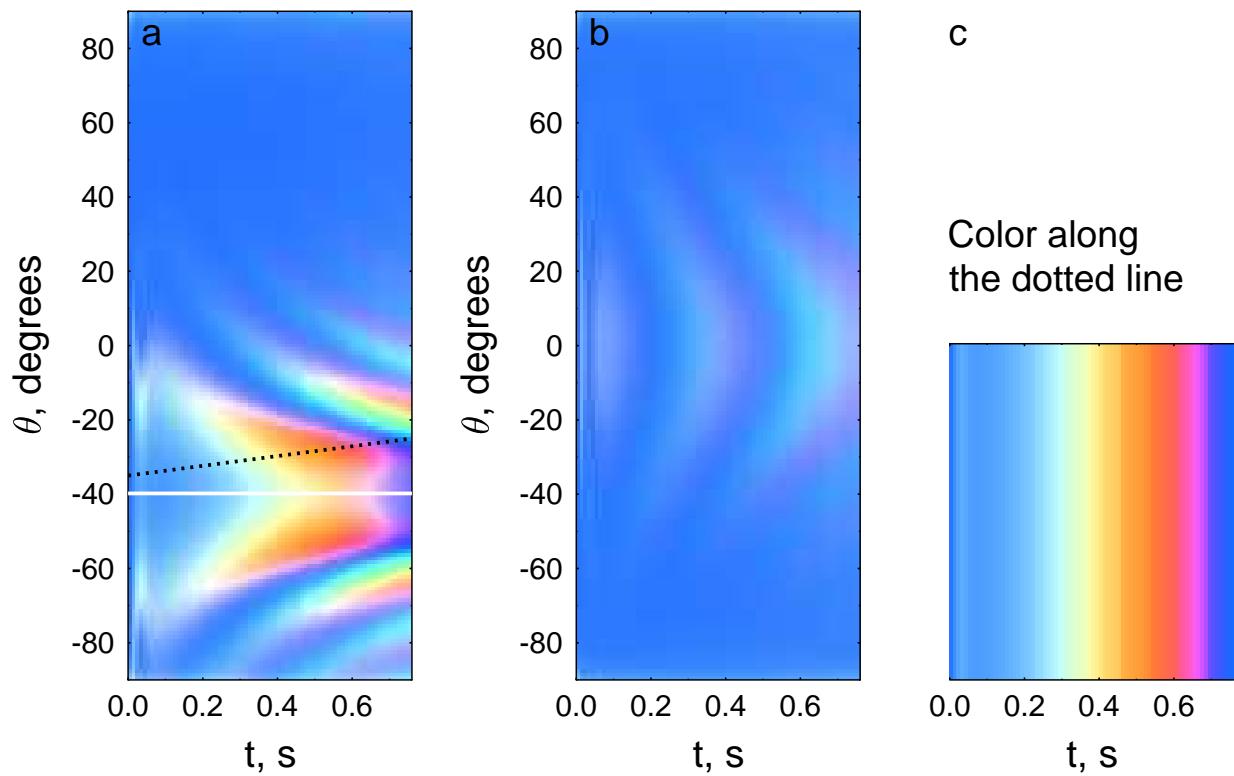


FIG. 8. Simulated radiances in the principal plane (a) and perpendicular to the principle plane (b) as a function of time t and viewing zenith angle θ . Colors are identical for viewing zenith angle 0° , where the viewing direction is identical (nadir). Thick white line marks the position of the sun, the dotted black line is one of many possible aircraft flight paths; (c) color sequence along the dotted black line.

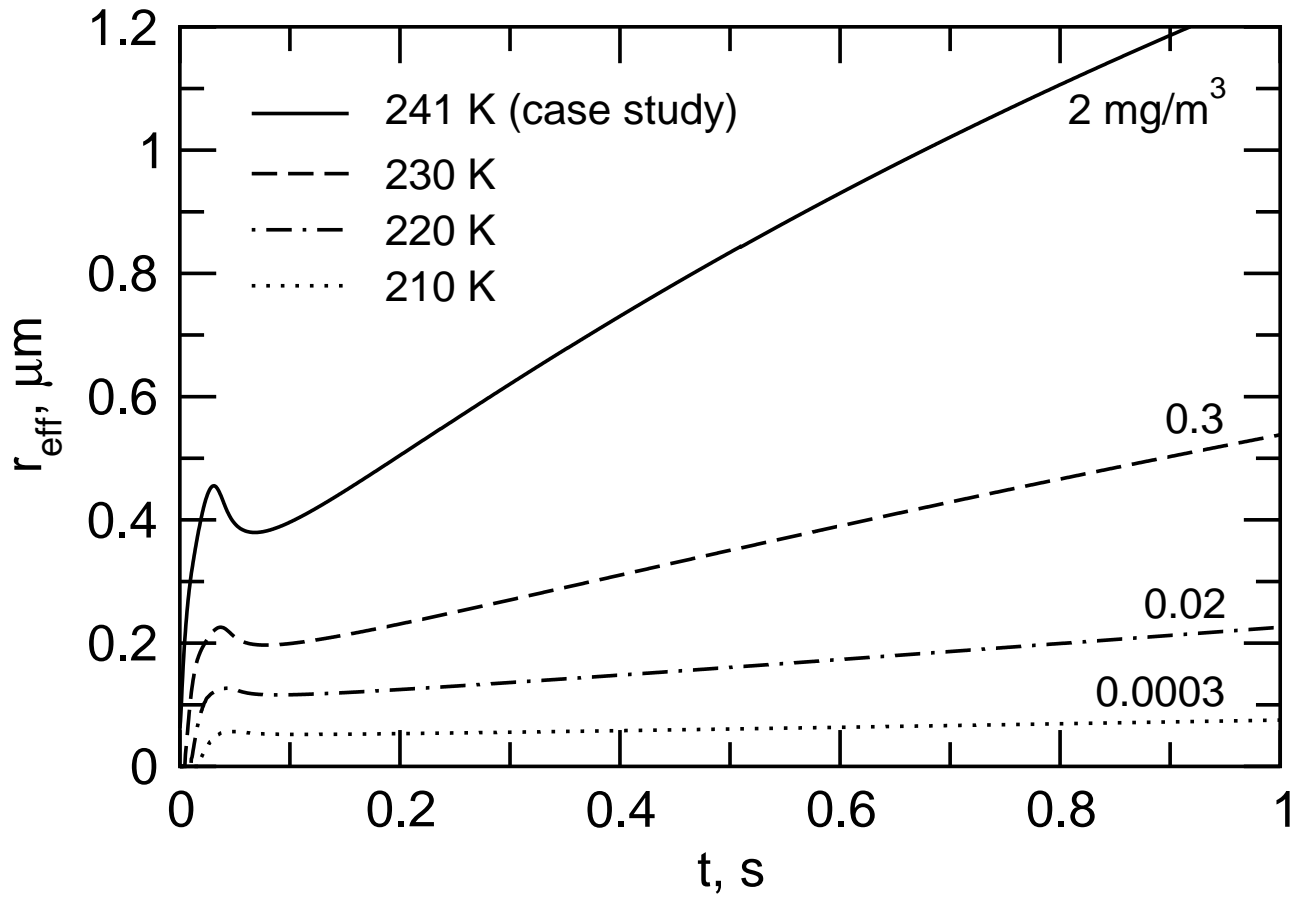


FIG. 9. Temporal evolution of effective ice particle radii r_{eff} for different ambient temperatures T_0 including the case study. Values have been taken along the $y = 3.2 \text{ m}$ trajectory. Labels denote the simulated ice water content at $t = 1 \text{ s}$.

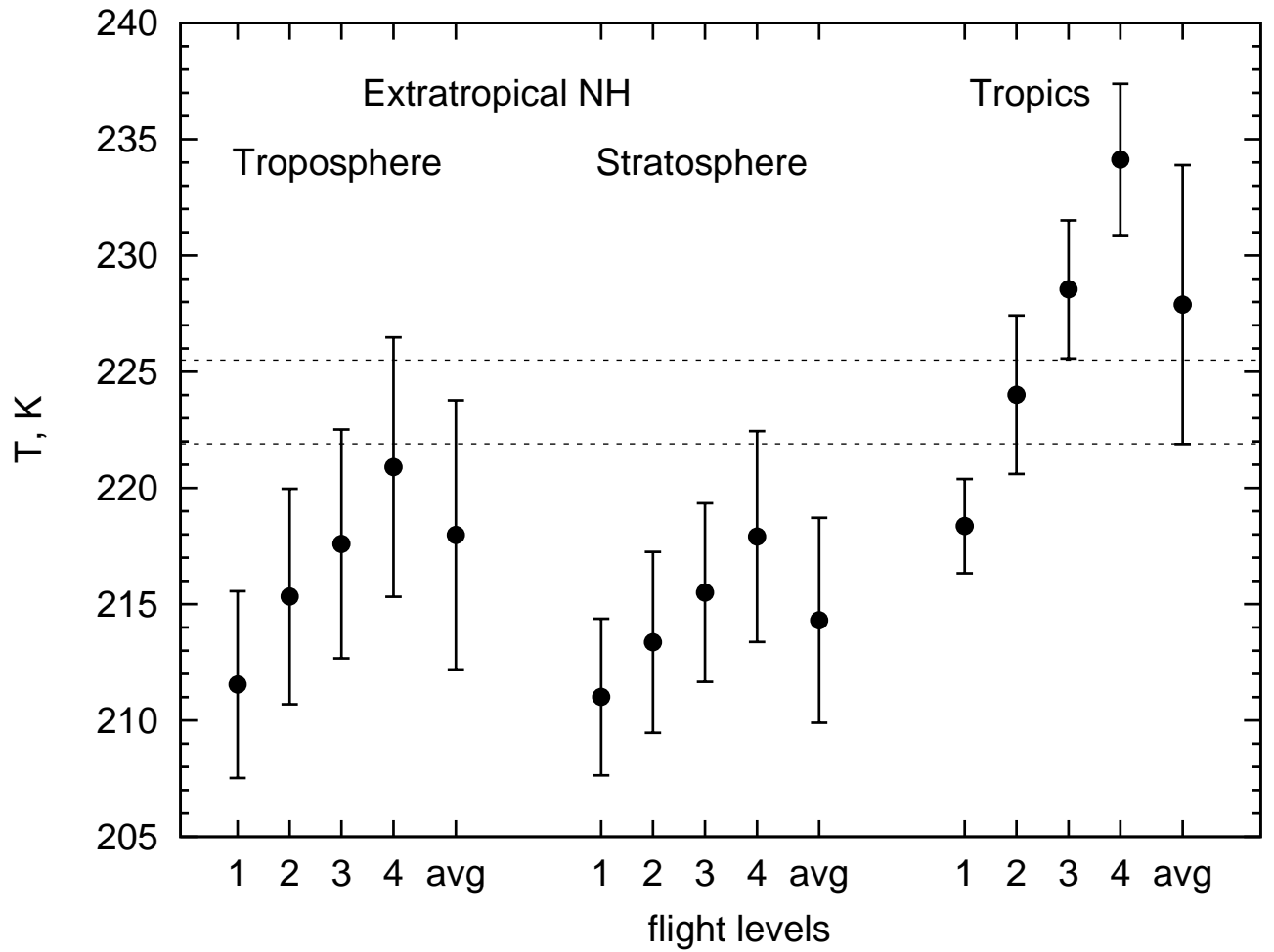


FIG. 10. Mean temperatures T (circles) measured onboard commercial aircraft based on MOZAIC data (1995-1999). Data are taken in ice-supersaturated regions covering the tropics ($0 - 30^\circ\text{N}$) and the northern extratropical upper troposphere and lowermost stratosphere. Labels 1, 2, 3, 4 correspond to pressure layers 190 – 209 mb, 210 – 230 mb, 231 – 245 mb, and 246 – 270 mb, respectively, and label ‘avg’ denotes the average over all layers. Average values have been weighted by the number of flights occurring in each layer. Temperatures are approximately normally distributed and the bars denote one standard deviation. The region between the two dotted lines marks the range of threshold temperatures below which jet contrails form in ice-saturated air within 190 – 270 mb and using a propulsion efficiency of 0.3. Figure adapted from Spichtinger (2004).

List of Tables

1	Properties of contrails forming at subsonic cruise altitudes (8 – 13 km). Numbers are approximate typical values. Concentrations and sizes refer to a time of 1 s after formation. Ice particle concentrations per meter of flight path are based on contrail cross-sections of 10 m ² and 100 m ² at the point of formation for jet exhaust and aerodynamic contrails, respectively. Jet contrails can only form at temperatures colder than 233 K at pressure altitudes below 300 mb. Ice particle concentrations and sizes in invisible aerodynamic contrails are much smaller than indicated.	52
---	---	----

TABLE 1. Properties of contrails forming at subsonic cruise altitudes (8 – 13 km). Numbers are approximate typical values. Concentrations and sizes refer to a time of 1 s after formation. Ice particle concentrations per meter of flight path are based on contrail cross-sections of 10 m² and 100 m² at the point of formation for jet exhaust and aerodynamic contrails, respectively. Jet contrails can only form at temperatures colder than 233 K at pressure altitudes below 300 mb. Ice particle concentrations and sizes in invisible aerodynamic contrails are much smaller than indicated.

	jet contrail	aerodynamic contrail
formation mechanism	isobaric mixing	adiabatic cooling
formation temperature	S_i -dependent	no restriction
formation time scale [ms]	500	40
formation length scale	wing span	wing depth
water vapor source	exhaust air	ambient air
ice nuclei	exhaust (mainly soot)	ambient (mainly liquid)
flow regime	turbulent	laminar
peak cooling rate [K/ms]	–1	–0.4
peak supersaturation	3	10
total ice particle concentration [cm ⁻³]	10 ⁴ – 10 ⁵	10 ² – 10 ³
ice particle concentration [m]	10 ¹¹ – 10 ¹²	10 ¹⁰ – 10 ¹¹
mean ice particle radius [μ m]	0.5 – 1	0.15 – 3
ice particle size distribution	moderately dispersed	nearly monodisperse
visible optical depth	0.5	> 0.01 (> 232 K)
visibility	visible	visible (> 232 K)